CHARACTERIZATION OF MAGHEMITE THIN FILMS PREPARED BY SOL-GEL PROCESSING

A THESIS SUBMITTED TO
THE GRADUATE SCHOOL OF NATURAL AND APPLIED SCIENCES
OF
MIDDLE EAST TECHNICAL UNIVERSITY

BY

AYLİN KARAKUŞCU

IN PARTIAL FULFILLMENT OF THE REQUIREMENTS
FOR
THE DEGREE OF MASTER OF SCIENCE
IN
METALLURGICAL AND MATERIALS ENGINEERING

OCTOBER 2006

Approval of the Graduate School of Natural and Applied Sciences

Prof. Dr. Canan ÖZGEN
Director

I certify that this thesis satisfies all the requirements as a thesis for the degree of Master of Science.

Prof. Dr. Tayfur ÖZTÜRK
Head of Department

This is to certify that we have read this thesis and that in our opinion it is fully adequate, in scope and quality, as a thesis for the degree of Master of Science.

Prof. Dr. Macit ÖZENBAŞ
Supervisor

Examining Committee Members

Prof. Dr. Muharrem TİMUÇİN	(METU,METE)
Prof. Dr. Macit ÖZENBAŞ	(METU,METE)
Prof. Dr. Mehmet PARLAK	(METU, PHYS)
Asst. Prof. Dr. Caner DURUCAN	(METU,METE)
Asst. Prof. Dr. Arcan DERİCİOĞLU	(METU,METE)

I hereby declare that all information in this document has been obtained and presented in accordance with academic rules and ethical conduct. I also declare that, as required by these rules and conduct, I have fully cited and referenced all material and results that are not original to this work.

Name, Last name : Aylin Karakuşcu

Signature :

ABSTRACT

CHARACTERIZATION OF MAGHEMITE THIN FILMS PREPARED BY SOL-GEL PROCESSING

Karakuşcu, Aylin
M.S., Department of Metallurgical and Materials Engineering
Supervisor: Prof. Dr. Macit Özenbaş

October 2006, 99 pages

In this study, maghemite (γ-Fe_2O_3) thin films were prepared by chemical solution deposition on glass and quartz substrates. The solution was prepared by using 0.3 M iron (III) nitrate [$Fe(NO_3)_3$ - $9H_2O$] as precursor and dissolved in a mixture of 2-methoxyethanol and acetylacetone in a molar ratio of 20:2, by stirring the solution at RT for 2 hours. Substrates were prepared by either piranha etching method or ultrasonic cleaning method. The solution was spin coated on glass and quartz substrates at 1400 and 4000 rpm for 1 minute. The resultant film thickness was found as 65 and 80 nm by SEM.

Viscosity of the main solution was found to be approximately as 0.0035 Pa.s by viscosity measurement. TGA/DTA analyses showed that, to produce maghemite thin film, heat treatment should be done between 330 °C and 440 °C.

Homogeneous and crack free maghemite thin films were observed by Energy Dispersive Spectrometry (EDS) and Scanning Electron Microscope (SEM) methods. TEM studies verified maghemite thin film formation by using electron diffraction and SAED (selected area electron diffraction) method. Thin film characteristics were evaluated by changing the experimental parameters which are annealing temperature, annealing time and thickness of the films using XRD (x-ray diffraction) method. Optical band gap of maghemite thin films were found as approximately 2.64 eV by UV-VIS Spectrophotometer. Magnetic properties of maghemite thin films were also examined by VSM (vibrating sample magnetometer).

Keywords: Iron oxide, maghemite, sol-gel, thin film.

ÖZ

SOL-JEL YÖNTEMİYLE HAZIRLANAN MAGHEMİT İNCE FİLMLERİN KARAKTERİZASYONU

Karakuşcu, Aylin
M.S., Metalurji ve Malzeme Mühendisliği Bölümü
Tez Yöneticisi: Prof. Dr. Macit Özenbaş

Ekim, 2006, 99 sayfa

Bu çalışmada, maghemit (γ-Fe_2O_3) ince filmler kimyasal çözelti biriktirme yöntemi kullanılarak cam ve kuars altlıklar üzerinde elde edilmişlerdir. Çözelti 0.3 M demir (III) nitratın 20:2 molar oranında karıştırılan 2-metoksietanol ve asetilaseton ile oda sıcaklığında 2 saat karıştırılması sonucunda hazırlanmıştır. Altlıklar piranha dağlama ya da ultrasonik temizleme yöntemiyle hazırlanmışlardır. Filmler, kaplama çözeltisinin cam ya da kuarts altlıklar üzerinde 1400 ile 4000 rpm hızlarında 1 dakika boyunca döndürülmesiyle (spin-coating) elde edilmişlerdir. Kaplanan filmlerin tek katman kalınlığı SEM kullanılarak 65 ve 80 nm olarak bulunmuştur.

Ana çözeltinin akışkanlık ölçümleri sonucunda akışkanlığı yaklaşık 0.0035 Pa.s olarak bulunmuştur. DTA ve TGA analizleri maghemit ince filmi oluşturmak için yapılan ısıl işlemin 330 °C ile 440 °C arası olması gerektiğini göstermiştir.

Homojen ve çatlak içermeyen ince filmler hazırlandığı EDS ve SEM yöntemleriyle görülmüştür. Maghemit ince filminin oluşumu TEM çalışmalarında, SAED ve elektron difraksiyon yöntemleri kullanılarak doğrulanmıştır. İnce filmlerin karakterizasyonu deneysel parametreler değiştirilerek XRD ile değerlendirilmiştir. Bu parametreler ısıl işlem sıcaklığı, süresi ve film kalınlığıdır. Maghemit ince filmlerinin enerji bant aralığı (enegy band gap) UV-VIS spektrofotometresi kullanılarak yaklaşık 2.64 eV olarak bulunmuştur. Maghemite ince filmlerinin manyetik özellikleri ise VSM (Titreşimli Nümune Manyetometresi) ile ölçülmüştür.

Anahtar Sözcükler: Demir oksit, ince film, maghemit, sol-jel.

To my family,

ACKNOWLEDGMENTS

I would like to first thank to my advisor, Prof. Macit Özenbaş. During the study, he has been a constant source of knowledge and support. I am grateful for sharing his experience and opinions throughout this period of work.

I am thankful to all the staff of the Department of Metallurgical and Materials Engineering especially my dear roommates Özge Acarbaş, Ali Erdem Eken and Volkan Kayasü.

I would like to express my sincere thanks to Dr. Erdem Yaşar from Kırıkkale University for TEM analyses and to Anadolu University, Department of Materials Science and Engineering for FE-SEM analysis. I am also grateful to the Department of Chemistry for their help in the measurement of optical properties and METU Central Laboratory for the analysis by TGA-DTA and viscosity measurement system. I want to send special thanks to Prof. Mürvet Volkan for selecting me as a project assistant for TUBİTAK project, which is also partially support this thesis.

Finally, I would like to express that I am so grateful to my family. I am thankful to my father, my mother, my grandmother, my grandfather and my sister Gamze for always being there for me. I would like to specially thank to my brother for always loving and supporting me and for being great role model.

TABLE OF CONTENTS

PLAGIARISM....iii

ABSTRACT.... ...iv

ÖZ vi

DEDICATION viii

ACKNOWLEDGMENTS ix

TABLE OF CONTENTS.... x

LIST OF TABLES xiii

LIST OF FIGURES xiv

CHAPTER

1. INTRODUCTION.... 1

2. LITERATURE SURVEY 4

    2.1 Iron Oxides.... 4

    2.2 Crystal Structures of Iron Oxides.... 4

        2.2.1 Magnetite 5

        2.2.2 Hematite.... 5

        2.2.3 Maghemite 5

    2.3 Magnetic Properties of Iron Oxides.... 6

        2.3.1 Diamagnetism 7

        2.3.2 Paramagnetism.... 7

        2.3.3 Ferrimagnetism 9

        2.3.4 Superparamagnetism 10

    2.4 Chemical Solution Deposition Technique 12

        2.4.1 Process Chemistry of Sol-Gel Processing 17

        2.4.2 Spin Coating Process 22

            2.4.2.1 Viscosity 24

        2.4.3 Drying and Annealing of Maghemite Thin Films 26

3. EXPERIMENTAL PROCEDURE 28

    3.1 Solution Preparation 28

    3.2 Preparation of Maghemite Thin Films 30

        3.2.1 Preparation of Substrates 30

            3.2.1.1 Piranha Solution 33

        3.2.2 Spin Coating 35

        3.2.3 Heat Treatment of Maghemite Thin Films 35

    3.3 Characterization of Solution 37

        3.3.1 Viscosity 38

        3.3.2 TGA/DTA 38

    3.4 Characterization of Maghemite Thin Films 39

        3.4.1 Structural and Morphological Analysis 39

        3.4.2 Optical Analysis 42

            3.4.2.1 Modified Envelope Method 42

        3.4.3 Magnetic Analysis 47

4. RESULTS AND DISCUSSION 48

    4.1 Solution Properties 50

4.2 Thin Film Preparation 56

4.3 Morphology of the Films 58

4.4 Structure of Maghemite Thin Films 63

4.4.1 Effect of the Annealing Temperature on the Maghemite Formation 63

4.4.1.1 XRD Study 64

4.4.1.2 TEM Study 65

4.4.2 Effect of the Annealing Time on the Maghemite Formation...72

4.4.2.1 XRD Study 73

4.4.3 Effect of Film Thickness on the Maghemite Formation 75

4.5 Parallel Beam Method.. 78

4.6 Optical Properties of Maghemite Thin Films.................................. 80

4.7 Magnetic Properties of Maghemite Thin Films 89

5. CONCLUSION AND FURTHER SUGGESTIONS................................. 91

REFERENCES... 95

LIST OF TABLES

TABLES

Table 2.1. Structural parameters for maghemite (γ-Fe_2O_3), hematite (α-Fe_2O_3) and magnetite (Fe_3O_4)....6

Table 2.2. Different production techniques which were used to prepare maghemite thin films....14

Table 2.3. The literature survey of the sol-gel processes which were used to produce maghemite, hematite and magnetite thin films....20

Table 3.1. Precursors and solvents used in this study....30

Table 4.1. Experimental details of the samples which were prepared during the study....49

Table 4.2. Approximate particle sizes of iron oxide powders obtained from the solutions....56

Table 4.3. The measured radii and calculated d_{hkl} of the sample (~80 nm) which was annealed at 350 °C for 1 hour....67

Table 4.4. The observed and theoretical interplanar spacings of the sample (~80 nm) which was annealed at 350 °C for 1 hour....68

Table 4.5. The measured radii and calculated d_{hkl} of the sample (~80 nm) which was annealed at 500 °C for 1 hour....70

Table 4.6. Literature survey for optical band gaps of different iron oxides....86

Table 4.7. Optical properties of thin film annealed at 500 °C for 1 hour....89

Table 4.8. Literature survey for saturation magnetization of maghemite thin films..91

LIST OF FIGURES

FIGURES

Figure 2.1. Representation of structures of magnetite (a) and maghemite (b); and corundum structure of hematite (c)..6

Figure 2.2. Different orientations of magnetic dipoles: (a) paramagnetic, (b) ferromagnetic, (c) antiferromagnetic, and (d) ferromagnetic.........7

Figure 2.3. Ground state and excited state of two metal ions, M_1 and M_2................10

Figure 2.4. Magnetization (*M*) vs. applied field (*H*) for ferromagnetic, paramagnetic and superparamagnetic materials 12

Figure 2.5. The chart of sol-gel process 16

Figure 2.6. Stages of the spin coating process...23

Figure 2.7. (a) Newtonian, (b) shear thinning and (c) shear thickening non Newtonian behaviors...25

Figure 3.1. The flow diagram of solution preparation used for the production of maghemite thin films...29

Figure 3.2. Routes for substrate preparation...32

Figure 3.3. The flow chart for the production of thin films......................................36

Figure 3.4. The schemetic diagram of parallel beam method...................................39

Figure 3.5. The schematic diagram of the x-ray equipment.....................................40

Figure 3.6. The schematic view of the measurement conditions of the parallel beam method...41

Figure 3.7. Schematic diagram of the modified envelope method: a weakly absorbing thin film on a completely transparent finite substrate……..……..44

Figure 4.1. Viscosity change of solution S1 at 20 °C with respect to shear rate........51

Figure 4.2. Viscosity change of solution S1 at 25 °C with respect to shear rate........52

Figure 4.3. TGA curve of the powder sample from solution S1 which was obtained after drying at 100° C for 8 h in air..53

Figure 4.4. DTA result of the powder sample from solution S1 which was obtained after drying at 100 °C for 8 h in air..54

Figure 4.5. XRD spectra of powders (annealed at 350 °C for 1 hour) obtained from the solutions S1, S2 and S3..55

Figure 4.6. SEM micrograph of glass substrate which was not etched......................57

Figure 4.7. SEM micrograph of etched glass substrate...57

Figure 4.8. EDS analysis of the etched glass substrate...58

Figure 4.9. SEM micrograph of a single layered film surface which was coated on a glass substrate...59

Figure 4.10. SEM micrograph of a multi-layered film surface which was coated on a glass substrate...59

Figure 4.11. Cross sectional SEM micrograph of the three-layered film (total thickness ~190 nm) which was coated at 4000 rpm.................60

Figure 4.12. Cross sectional SEM micrograph of the single-layered film (~80 nm) on a glass substrate coated at 1400 rpm..61

Figure 4.13. Cross sectional FE-SEM micrograph of the single-layered film (~80 nm) on a glass substrate coated at 1400 rpm..61

Figure 4.14. EDS analysis of three-layered film (~190 nm) which was annealed at 400 °C for 1 hour..62

Figure 4.15. EDS analysis of single-layered film (~65 nm) which was annealed at 400 °C for 1 hour..63

Figure 4.16. XRD spectra of single layered thin films (~80 nm) annealed at different temperatures for 1 hour..64

Figure 4.17. (a) TEM micrograph and (b) electron diffraction pattern of the single-layered maghemite thin film (~80 nm) which was annealed at 350 °C for 1 hour..66

Figure 4.18. Electron diffraction pattern and its interpretation for single layered (~80 nm) maghemite thin film which was annealed at 350 °C for 1 hour....68
Figure 4.19. (a) TEM micrograph and (b) electron diffraction pattern of single layered (~80 nm) maghemite thin film which was annealed at 350 °C for 1 hour....69

Figure 4.20. (a) TEM micrograph and (b) selected area electron diffraction (SAED) pattern of the single layered film (~80 nm) which was annealed at 500 °C for 1 hour....70

Figure 4.21. Selected area electron diffraction pattern (SAED) of the film which was annealed at 500 °C for 1 hour....71

Figure 4.22. (a) TEM micrograph and (b) selected area electron diffraction (SAED) pattern of the film which was annealed at 500 °C for 1 hour....72

Figure 4.23. XRD spectra of single layered (~80 nm) thin films which were annealed at different temperatures for 4 hour....73

Figure 4.24. XRD spectra of single-layered (~80 nm) thin films which were annealed at 400 °C for different periods....74

Figure 4.25. XRD spectra of single-layered (~80 nm) thin films annealed at 350 °C for different periods....75

Figure 4.26. XRD spectra of single (~65 nm) and 5-layered (~300 nm) thin films annealed at 400 °C for 1 hour....76

Figure 4.27. XRD spectra of single (~80 nm) and 20-layered (~1.5 μm) thin films annealed at 350 °C for 1 hour....77

Figure 4.28. XRD spectra of single (~80 nm) and twenty-layered (~1.5 μm) films annealed at 350 °C for 1 hour and 4 hours, respectively....78

Figure 4.29. XRD spectra of maghemite thin film (~80 nm) which was annealed at 350 °C for 1 hour....79

Figure 4.30. XRD spectra of thin film (~80 nm) which was annealed at 400 °C for 1 hour....80

Figure 4.31. UV-visible spectra of thin films (~80 nm) annealed at different Temperatures....81

Figure 4.32. UV-visible spectra of the maghemite thin film (~80 nm) annealed at 350 °C for 1 hour....82

Figure 4.33. The change in absorption coefficient with changing *hv* of maghemite thin film which was annealed at 350 °C..83

Figure 4.34. The change in absorption coefficient with changing *hv* of thin film which was annealed at 400 °C..84

Figure 4.35. Plot of $(\alpha h\nu)^2$ versus photon energy of maghemite thin film which was annealed at 350 °C..84

Figure 4.36. Plot of $(\alpha h\nu)^2$ versus photon energy of thin film which was annealed at 400 °C..85

Figure 4.37. Extinction coefficient versus wavelength of maghemite thin film which was annealed at 350 °C..86

Figure 4.38. Extinction coefficient versus wavelength of maghemite thin film which was annealed at 400 °C..87

Figure 4.39. Optical transmission spectra of the thin film, which was annealed at 500 °C, on glass substrate...88

Figure 4.40. The M - H curve of maghemite thin film (~200 nm) annealed at 350 °C for 1 hour..90

Figure 4.41. The M – H curve of single layered thin film (~80 nm) annealed at 600 °C for 1 hour..91

CHAPTER 1

INTRODUCTION

In the last decade, increased investigations with several types of iron oxides have been carried out in the field of nanosized magnetic particles (mostly maghemite, γ-Fe_2O_3, hematite α-Fe_2O_3 or magnetite, Fe_3O_4, single domains of about 5–20 nm in diameter) [1], among which maghemite is a very promising candidate because of its enhanced magnetic, mechanical properties and superior recording characteristics. In general, Fe_2O_3 is a suitable material for gas sensors, photoelectrodes and humidity sensors in α-phase and hematite is very weakly ferrimagnetic whereas γ-phase is ferrimagnetic. γ- Fe_2O_3 has spinel crystal structure, whereas α-Fe_2O_3 has corundum structure where the oxide ions form a hexagonally close packed array with Fe^{+3} ions occupying the octahedral interstices. Conversion from one form to the other is possible by oxidation or reduction mechanism.

Maghemite is a ferrimagnetic iron oxide crystal that has many applications in the magnetic recording media. It is an important magnetic oxide used to coat cassettes and floppy disks. Because of the small coercivity of γ-Fe_2O_3 nanoparticles, which arises from a negligible barrier in the hysteresis of the magnetization loop, they can also be used in magneto-optical devices [2]. Moreover, maghemite is technologically important, as it is being used widely for the production of ferrofluids and catalysts. Nanophase maghemite, often found in the corrosion coatings of atmospherically exposed structural steels, has particle size of the order of nm and exhibit superparamagnetic behavior.

Computer systems have increasingly become smaller and smaller, and have begun to test the limits of current technology in terms of processing. Hard drives, specifically, are reaching their maximum storage capacity due to the effect of superparamagnetism, in which the magnetization state of a bit spontaneously switches from heat energy, and external magnetic forces from other bits. One way to prevent this, and allow higher data densities, is to use patterned magnetic recording media. One of the most efficient ways to pattern the media is the self assembling process of maghemite thin films. As a result, recently considerable attention has been given to the preparation of γ- Fe_2O_3 thin films for high density magnetic recording disk applications because of their enhanced magnetic, mechanical properties and superior recording characteristics [3].

Various methods have been reported for the synthesis of maghemite thin films, such as chemical vapour deposition (CVD) [4-6], sputtering [7, 8], hydrothermal deposition [9], metal organic deposition [10] or oxygen-plasma assisted molecular beam epitaxy (MBE) [11]. Among the wet chemical deposition techniques, the sol-gel process has become one of the successful techniques for preparing iron oxide films [12, 13]. The sol-gel process can exhibit a number of advantages over the physical deposition techniques. One advantage of the sol-gel process is that it has the ability to tailor the film microstructure. By sol-gel method, highly uniform films can be prepared satisfactorily [13]. The process is an economical method for the preparation of single or composite metal oxide films as well as a relatively easy way to form large-area films [14]. Most importantly, sol-gel processing uses solutions prepared at low temperature rather than high temperature processing to make materials with controlled properties. Since maghemite (γ-Fe_2O_3) transforms to hematite at elevated temperatures, sol-gel process is one of the unique process for maghemite production. Moreover, sol-gel process is well suited for the preparation of maghemite thin films because of the use of liquid solutions at room temperature, which is a great advantage [15].

Sol-gel film processing involves the synthesis of a gel-precursor solution, or sol, which is applied to a substrate using spin-on or dip-coating techniques; the resulting gel layer is then heat treated to form a ceramic film. Generally, such treatments are carried out in two stages, by employing a hot plate heat treatment (drying step) at a temperature such as 100 °C, followed by a final heat treatment (annealing) at temperatures between 300 °C and 500 °C [16].

The aim of the thesis was to produce maghemite thin films and characterize with several methods. During this study, maghemite phase was observed below the annealing temperature of 400 °C for short annealing times. With increase in annealing temperature and time maghemite phase transforms to hematite phase which is weakly magnetic.

This report begins with a literature survey of maghemite thin films. First, a general description of iron oxide phases which are maghemite, hematite and magnetite were given to explain the terms that were used during characterization. Their crystal structures and magnetic properties are given. In the last part of Chapter 2, production of maghemite thin films by chemical solution deposition was explained with details of the process. Third chapter includes the experimental procedure consisting of solution preparation, coating of samples and characterization of the films. In the fourth chapter, presentation and discussion of the experimental results on solution preparation, film deposition and annealing procedure were given. Characterization of the solution by thermal analysis with TGA (Thermogravimetry) and DTA (Differential Thermal Analysis) and viscosity measurements were explained. In addition, microstructural characterization of thin films by XRD (x-ray diffraction), film microstructure and morphology characterization by SEM (scanning electron microscopy) and TEM (transmission electron microscopy), optical characterization by UV-Vis and magnetic characterization by VSM (vibrating sample magnetometer) were also explained in this part. Finally, the last chapter includes the conclusion and further suggestions related to the present work.

CHAPTER 2

LITERATURE SURVEY

2.1. Iron Oxides

Iron oxides play an important role in variety of disciplines, including corrosion science, chemistry, medicine, industrial chemistry, soil science and material science due to their interesting magnetic properties. Iron oxide can exhibit several crystal structures and compositions but the most important ones are maghemite (γ-Fe_2O_3), hematite (α-Fe_2O_3) and magnetite (Fe_3O_4) [17].

2.2. Crystal Structures of Iron Oxides

The basic structural unit for all Fe oxides is an octahedron, in which each Fe atom is surrounded either by six O or both O and OH ions. The O and OH ions form layers which are either approximately hexagonally close-packed (HCP) as e.g. in hematite or approximately cubic close-paced (CCP) as e.g. in maghemite. In both HCP and CCP structures, tetrahedral interstices also exist between three O or OH in one plane and anion in plane above. The HCP-forms, hematite, is termed α-phase, whereas the corresponding CCP-form, maghemite, is termed γ-phase. The α-phase is more stable than γ-phase [17].

2.2.1. Magnetite

In the cubic structure of both magnetite and maghemite 1/3 of the interstices are tetrahedrally coordinated with oxygen and 2/3 are octahedrally coordinated. Magnetite is a spinel structure. The tetrahedral positions are completely occupied by Fe^{3+}, the octahedral ones by equal amounts of Fe^{3+} and Fe^{2+} [17].

2.2.2. Hematite

Hematite crystallizes in the rhombohedral system, and it has the same crystal structure as corundum. Hematite consists of layers of FeO_6 octahedra which are connected by edge- and face-sharing (as in corundum) and stacked perpendicular to c direction. Two thirds of the octahedral interstices are filled with Fe^{3+}. The face-sharing is accomplished by a slight distortion of the octahedral which causes a regular displacement of the Fe ions. The distortion and the absence of H bonds yield a compact structure which is responsible for the high density of 5.26 g cm^{-3} [17].

2.2.3. Maghemite

Maghemite is an inverse spinel cubic structure. In maghemite only 5/6 of the total available positions are filled and only by Fe^{3+} the rest are vacancy ($\square$) (i.e. $Fe_{2.67}\square_{0.33}O_4$). Maghemite can have different symmetries depending on the degree of ordering of the vacancies. Completely ordered maghemite has a tetragonal symmetry, otherwise it is cubic. Figure 2.1 shows the unit cell corresponding to magnetite, hematite, and maghemite. Table 2.1 also lists the structural parameters for these iron oxides [17].

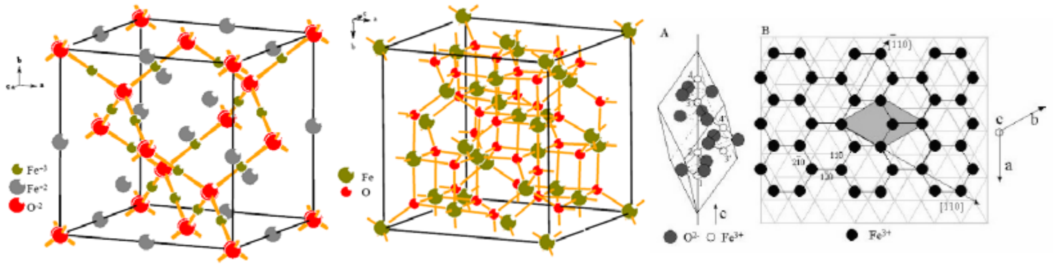

a b c

Figure 2.1. Representation of structures of magnetite (a) and maghemite (b); and corundum structure of hematite (c) [18].

Table 2.1. Structural parameters for maghemite (γ-Fe_2O_3), hematite (α-Fe_2O_3) and magnetite (Fe_3O_4) [19].

Compound	**Structural Type**	**Lattice Parameter**	**Geometry and Its Fraction**	**Remark**
Hematite (α-Fe_2O_3)	Hexagonal (R3c), Corundum	a=0.504 c=1.375	Distorted Octahedral Fe^{3+}	Antiferromagnetic
Maghemite (γ-Fe_2O_3)	Cubic ($P4_132$), Defect Spinel	a=0.835	Octahedral Fe^{3+} (5/8) Tetrahedral Fe^{3+} (3/8)	Ferrimagnetic
Magnetite (Fe_3O_4)	Cubic (Fd3m), Spinel	a=0.840	Octahedral Fe^{3+}, Fe^{2+} (2/3) Tetrahedral Fe^{3+} (1/3)	Ferrimagnetic

2.3. Magnetic Properties of Iron Oxides

There are various forms of magnetism that arise depending on how the dipoles interact with each other. Figure 2.2 shows a schematic presentation of the different types of arrangements of magnetic dipoles.

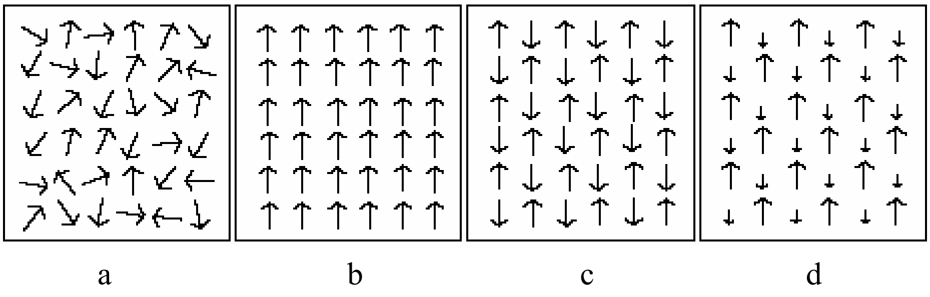

Figure 2.2. Different orientations of magnetic dipoles: (a) paramagnetic, (b) ferromagnetic, (c) antiferromagnetic, and (d) ferrimagnetic [18].

2.3.1. Diamagnetism

Diamagnetism is a very weak form of magnetism that is only exhibited in the presence of an external magnetic field. It is the result of changes in the orbital motion of electrons due to the external magnetic field. The induced magnetic moment is very small and in a direction opposite to that of the applied field. When placed between the poles of a strong electromagnet, diamagnetic materials are attracted towards regions where the magnetic field is weak. Diamagnetism is found in all materials; however, because it is so weak it can only be observed in materials that do not exhibit other forms of magnetism. Also, diamagnetism is found in elements with paired electrons [20].

2.3.2. Paramagnetism

Paramagnetism is the tendency of the atomic magnetic dipoles, due to quantum-mechanical spin as well as electron orbital angular momentum, to align with an external magnetic field. Paramagnetic materials attract and repel like normal magnets when subject to a magnetic field. This alignment of the atomic dipoles with the magnetic field tends to strengthen it, and is described by a relative magnetic permeability greater than unity (or, equivalently, a small positive magnetic susceptibility).

Paramagnetism requires that the atoms individually have permanent dipole moments even without an applied field, which typically implies a partially filled electron shell. In pure paramagnetism, these atomic dipoles do not interact with one another and are randomly oriented in the absence of an external field, resulting in zero net moment. If they do interact, they can spontaneously align or anti-align, resulting in ferromagnetism (permanent magnets) or antiferromagnetism, respectively. Paramagnetic behaviour can also be observed in ferromagnetic materials that are above their Curie temperature, and in antiferromagnets above their Neel temperature.

Under relatively low magnetic field saturation when the majority of the atomic dipoles are not aligned with the field, paramagnetic materials exhibit magnetisation according to Curie's Law:

$$M = C \cdot \frac{B}{T} \qquad \text{Eq. [2.1]}$$

where M is the resulting magnetization, B is the magnetic flux density of the applied field, T is absolute temperature, C is a material-specific Curie constant.

This law indicates that paramagnetic materials tend to become increasingly magnetic as the applied magnetic field is increased, but less magnetic as temperature is increased. Curie's law is incomplete because it fails to predict the saturation that occurs when most of the atomic dipoles are aligned (after everything is aligned, increasing the external field will not increase the total magnetization). So the Curie constant, really should be expressed as a function of how much of the material is already aligned.

Paramagnetic materials in magnetic fields will act like magnets but when the field is removed, thermal motion will quickly disrupt the magnetic alignment. In general paramagnetic effects are small (magnetic susceptibility of the order of 10^{-3} to 10^{-5}) [21].

2.3.3. Ferrimagnetism

In many ionic crystals the exchange energy, J, between the spins of two neighbouring atoms is negative. This occurs due to the fact that the spin of the shared electron from the metal ions with the oxygen follows Pauli's principle. Thus, if the metal ion has an outer shell less than half occupied all the spins will be aligned parallel inside the shell and antiparallel with respect to the other metal ion. This means that antiparallel arrangement is the one that provides with lowest energy.

In the case of spinel ferrites, the metal ions in the unit cell exist in 8 tetrahedral and 16 octahedral positions, where the metal ions are arranged into two sublattices A and B corresponding to tetrahedral and octahedral places. Neutron diffraction studies showed that there are two types of spinel ferrites: normal and inverse. Studies showed that the normal spinel ferrites are paramagnetic whereas the inverse spinel ferrites behaved as ferrimagnetic. In the case of normal spinel ferrites, the divalent metal ions are located in the sublattice A and the iron (III) ions are located in the sublattice B; whereas in the case of inverse spinel ferrites one half of the iron (III) ions occupy the sublattice A with the sublattice B occupied by the other half of iron (III) ions and the divalent metal ions.

In spinel iron oxides, the metallic ions are separated by an oxygen (II) ion and since the distance between the metallic ions is too large, it was proposed that there is a superexchange between the metallic ions through the oxygen ion. Figure 2.3 shows a schematic representation of the superexchange interactions between two metal ions through oxygen.

The net magnetic moment of the material is the difference in magnetic moments of sublattices A and B, which explained why the magnetic moment per formula unit was lower than the otherwise expected value. Thus, the higher the magnetic moment of the divalent cation is, the higher the magnetisation [18].

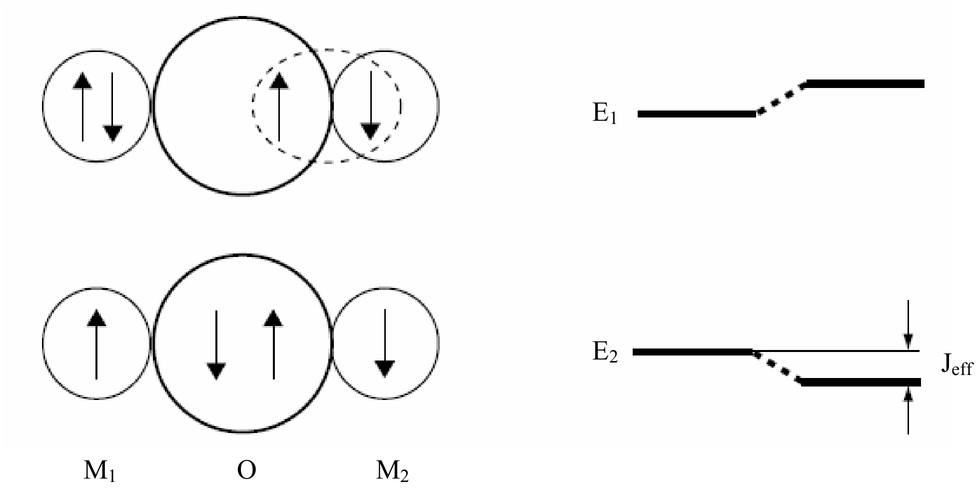

Figure 2.3. Ground state and excited state of two metal ions, M_1 and M_2. The spin configurations as drawn become intermingled, causing an extra reduction of ground state energy; this does not occur if M_1 and M_2 have parallel spins [18].

2.3.4. Superparamagnetism

Below the Curie temperature of ferromagnet or ferrimagnet, all the spins are coupled together and so cooperate to yield a large total moment. This moment is bound rigidly to the particle by one or more of the variety of anisotropies and the energy of this bond is KV where K is the anisotropy constant and V is the volume of the particle. With decreasing particle size, KV decrease until the thermal energy kT can disturpt the bonding of the total moment to the particle. Then this moment is free to move and respond to an applied field independent of the particle. This moment is the moment of the particle and equal to

$$\mu_P = M_S V \qquad \text{Eq. [2.2]}$$

where μ_p is the permeability of the particle and M_s is the saturation magnetization.

Moment of the particle can be quite large, thousands of Bohr magnetons. An applied field would tend to align this giant (or super) moment, but kT would fight the alignment just as it does in paramagnet. Thus, this phenomenon is called superparamagnetism.

If the anisotropy is zero or very weak, one would expect that the total moment could point in any direction. If K is significantly greater than zero, μ could appoint in either of two directions along the easy axis. However both these are an approximation to M versus H for a real superparamagnet because the system of the particles is no doubt polydisperse, so that there is a distribution of μ_p values, and the particles would most likely have random orientation, hence random easy axes [22].

The phenomenon of superparamagnetism is, in fact, timescale-dependent due to the stochastic nature of the thermal energy. The anisotropy energy KV represents an energy barrier to the total spin reorientation; hence the probability for jumping this barrier is proportional to the Boltzmann factor.

$$\exp(-KV/kT) \qquad \text{Eq. [2.3]}$$

In Figure 2.4, various forms of magnetism are shown on a hysteresis loop. Where M_S is saturation magnetization at which all the spins are aligned with the magnetic field; H_C is the coercive field which is the internal magnetic field of material; M_R is the remanent magnetization which is the magnetization retained by the material. It can be seen form the figure that superparamagnetic and paramagnetic materials do not have a hysteresis loop.

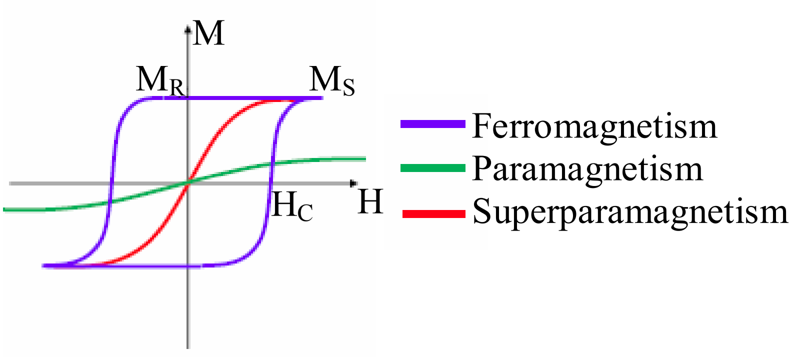

Figure 2.4. Magnetization (*M*) vs. applied field (*H*) for ferromagnetic, paramagnetic and superparamagnetic materials [23].

Hematite is an antiferromagnetic material below the Morin transition at 260 K, and weakly ferromagnetic above the Morin transition, which is a transition specific to α-Fe_2O_3. In Morin transition there is a change in the direction of the atomic magnetic moments in the antiferromagnetic state from parallel to perpendicular to the c-axis. However magnetite is a ferrimagnetic material which has the Curie temperature about 580 °C. Maghemite is ferrimagnetic but characterized by the superparamagnetic relaxation phenomenon, which is strongly affected by particle size, shape and by various surface effects. The interesting magnetic properties of nanostructured maghemite are due to finite size effects and/or high surface/volume ratios, thus making the study of the interrelation between microstructure and magnetism very appealing [24].

2.4. Chemical Solution Deposition Technique (CSD)

Many techniques have been used for the preparation of maghemite thin films. The production techniques (other than sol-gel processing) used to prepare maghemite thin films are given in Table 2.2. Sol-gel processing is a relatively new method and appears to be very promising because of the apparent ease of control of chemical uniformity at the molecular level providing that the proper precursors are used and the heat treatment is carefully carried out. The entire sol-gel process begins with the preparation of the liquid solution having the most ideal structural groups corresponding to that in the crystalline solid, maintaining proper liquidity just prior to the deposition onto the substrate, dipping or spin-coating in a controlled atmosphere and then heat treatment also under controlled atmospheres [25].

Table 2.2. Different production techniques which were used to prepare maghemite thin films

Production method	**Precursor / Target**	**Experimental details**	**Substrate**	**Ref. no**
MOCVD	Iron acetyl acetonate complex	T > 500 °C	Cleaned glass (Corning 7059)	5
CVD	Iron acetyl acetonate complex + Co(acac)$_3$	Substrates preheated to 300-450 °C under Ar to form α -Fe_2O_3, then oxidation at 350°C under H_2 to obtain γ-Fe_2O_3	Cleaned glass (Corning 7059)	6
Sputtering	Pure iron target Os doped iron target	γ-Fe_2O_3 T>300 °C γ-Fe_2O_3 production: 1. The α-phase of Fe_2O_3 rf sputtering + reduction to Fe_3O_4 2. Oxidation to γ-Fe_2O_3 3. Direct sputtering Fe_3O_4+oxidation to γ-Fe_2O_3	(100) Si Al-Mg alloy substrate	7, 8
Hydrothermal deposition	$Fe(NO_3)_3.9H_2O$ + $CoCl_2$.$6H_2O$	Fe_3O_4 films oxidized at 400°C in air for 2 h	α –Al_2O_3 for XRD silicon substrates	9
Metal organic deposition	$Fe(NO_3)_3.9H_2O$-acetylacetonate+ isopropanol	15 min at 365°C	Quartz plates	10
Oxygen-plasma assisted molecular beam epitaxy (MBE)	Epitaxial films of α -Fe_2O_3 (0001) were prepared on Pt(111) which was deposited on $A1_2O_3$(0001) at 600°C	γ-Fe_2O_3 (001) and Fe_3O_4 (001) were grown on MgO (001)	Polished α –Al_2O_3 (0001) and MgO (001) single crystals	11

There are many advantages of sol-gel processing. It does not only allow for materials to have an oxide composition, but it also permits the production of new hybrid organic-inorganic materials which do not exist naturally. Sol-gel processing also has other advantages like very pure products can be obtained by simply purifying the precursors either by distillation, crystallization or electrolysis.

There are other more fundamental advantages related to sol-gel processing. For instance, the kinetics of the various chemical reactions can be easily controlled by the low processing temperatures and by the often dilute conditions. The nucleation and growth of the primary colloidal particles can also be controlled in order to give particles with a given shape, size and size distribution.

The sol-gel process is particularly suited for the preparation of thin films. Not only is the use of liquid solutions at room temperature a great advantage but theoretically, if the techniques of preparation of multicomponent homogeneous liquid solutions are available, just about any crystalline and non-crystalline films can be applied to many substrates. Although the preparation of relatively large monolithic samples by the sol-gel method is both costly because of raw materials and difficult because of porosity and large shrinkages, the formation of thin films is free from such problems [26].

Precipitation and co-precipitation techniques are also used and are sometimes even considered as a side branch of sol-gel processing. The chemical reactions concerned in this case are the same as those occurring in sol-gel synthesis; they lead to the production of colloidal particles, but can also be dispersed into a stable sol [25].

Many variations can be brought to the sol-gel synthesis of ceramics. In fact, sol-gel processing does not only designate a unique technique, but a very broad type of procedures that centralizes around a single scheme as presented in Figure 2.5. The first step of any sol-gel process always consists in selecting the precursors of the required materials. It is the precursor that, by its chemistry, leads the reaction towards the formation of either colloidal particles or polymeric gels. When the future material is composed of several components (i.e., when several oxides are mixed together), then the use of a combination of different precursors and procedures enhances different chemical synthesis and hence different products. The colloidal particles obtained can then be precipitated and treated according to one of the conventional processing techniques, such as cold pressing, hot-pressing and sintering, in order to produce the desired ceramic. Sols and gels can also be spinned into fibers or transformed through one of other various techniques into a coating material. If a gel powder for melting purposes is required, than the gel may be dried and no special cares need. On the other hand, controlled gelation and drying leads to the formation of monosized droplets which can reach several hundred micrometers in diameter. Furthermore, the size of pores can also be controlled by supercritical drying or by the use of surfactants [25].

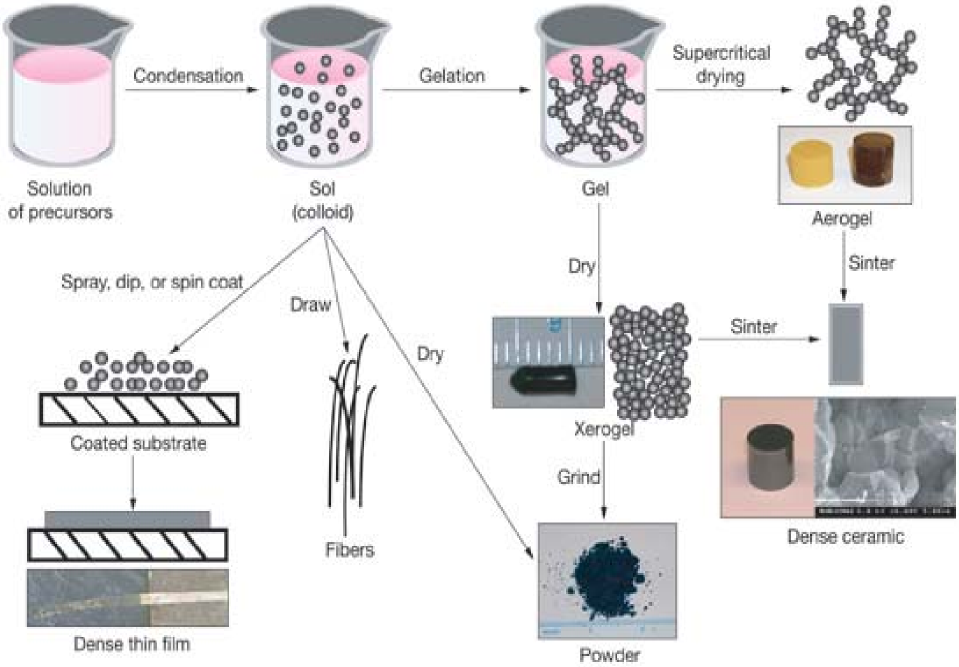

Figure 2.5. The chart of sol-gel process [27].

2.4.1. Process Chemistry of Sol-Gel Processing

As it can be seen from the Figure 2.5, the sol-gel process can be categorized into three routes. The first one called “colloidal” method involves the dispersion of colloidal particles in a liquid to form a sol and then the destabilization of the sol to produce a gel which is subsequently dried, to form a porous ceramic, and fired to crystallize and/or densify the material [28]. The second method involves the production of powders precipitated from the sol. The resulting powders are then dried and processed using traditional ceramic processing techniques. The third approach is the polymerization of organometallic compounds such as alkoxides to produce a gel with a continuous network [29].

A “colloid” is a suspension in which the dispersed phase is so small that gravitational forces are negligible and interactions are dominated by short-range forces, such as van der Waals attractions and surface charges. The inertia of dispersed phase is so small enough that it exhibits Brownian motion, a random walk driven by momentum imported by molecules of the suspending medium. A “sol” is a colloidal suspension of solid particles in a liquid [30].

Metal oxides are members of the family of metallorganic compounds, which have an organic ligand attached to a metal or metalloid atom. Organometallic compounds are defined as having direct metal-carbon bonds, not metal-oxygen-carbon linkages as in metal alkoxides; thus alkoxides are not organometallic compounds, although that usage turns up frequently in the literature. Metal oxides; are popular precursors because they react with water. The reaction is called hydrolysis, because a hydroxyl ion becomes attached to the metal atom

$$M(OR)_x + H_2O \rightarrow M(OH)_x + xROH \qquad \text{Eq. [2.4]}$$

Two partially hydrolyzed molecules can link together in a condensation, such as

$$(OR)_{x-1}M - OH + HO - M(OR)_{x-1} \rightarrow (OR)_{x-1}M - O - M(OR)_{x-1} + H_2O \quad \text{Eq. [2.5]}$$

or

$$(OR)_{x-1}M-OR+HO-M(OR)_{x-1}\rightarrow(OR)_{x-1}M-O-M(OR)_{x-1}+ROH \qquad \text{Eq. [2.6]}$$

These reactions cause the formation of a metal-oxygen-metal bridge, which constitutes the backbone of any oxide ceramic structure. Continued condensation leads to an increase in the density of metal-oxygen-metal crosslinks until eventually gelation or precipitation occurs [31].

The basic principle of the sol-gel process is to form a solution of the elements of the desired compounds in an organic solvent, polymerize the solution to form a gel, and dry and fire this gel to displace the organic components and form a final inorganic oxide.

Important and typical precursors for making sol-gel solutions are alkoxides of the general composition $M(O\text{-}R)_n$, where R is an alkyl radical (CH_3, C_2H_5, etc.). Their properties and reactions affect the preparation process and determine the product features. Inorganic and organic salts can also be used for introducing some oxides into multicomponent systems. The precursors are dissolved in a suitable organic solvent to form the solution. In order to get the solution with a high concentration of necessary components and proper viscosity, surface tension and boiling point, the solvent must be carefully selected.

In order to obtain a suitable solution for making films, various properties of solution are adjusted. Different alkoxides of different elements show a wide range of reactivity toward H_2O which makes the preparation of multicomponent homogeneous systems difficult and also presents difficulties with premature gelation during film processing. This can be overcome by adding a chelating organic ligand into the solution to control the hydrolysis rates of highly reactive alkoxide. The gelation of a solution means the formation of a network in the solution. The hydrolysis and polycondensation of organometallic compounds such as alkoxides leads gelation. During the drying stage the wet coating is converted to a relatively dry, harder coating and considerable shrinkage of the coating occurs. It is at this stage that problems related to film cracking and surface smoothness in the final film become most acute.

The annealing step converts the gel coating into a densified complex oxide film. This process includes the removal of residual –OH or –OR groups by polycondensation reactions, pyrolysis of the organic compounds or groups left in the film into carbon, oxidation of the carbon, and gradual densification of the film [32].

Since works on the synthesis of maghemite thin films by sol–gel method have been rarely reported up to date, some valuable information about maghemite thin film formation and characterization was gathered from the studies on magnetite thin films and hematite thin films. Table 2.3 summarizes the details of the sol-gel processes which were used to produce maghemite, hematite and magnetite thin films taken from the literature.

Table 2.3. The literature survey of the sol-gel processes which were used to produce maghemite, hematite and magnetite thin films.

Formed phases	Solvent and precursor	Experiment details	Drying time and temperature	Annealing time and temperature	Substrate	One-layer thickness	Ref. no
γ-Fe_2O_3	Iron(III) nitrate +sodium methoxide +ethylene glycol +2-methoxyethanol +polyethylene glycol	T = 70 °C Iron nitrate 10-15 wt% μ= ~10 mPas	100°C for 10 min	350-600°C under air or N_2 Heating rate 5°C/min	*Si for magnetization measurement *Glass for XRD, SEM	120 nm	33
γ-Fe_2O_3	Iron(III) nitrate +ethylene glycol	T=80 °C under N_2 Iron nitrate 15 wt%	110°C for 15 min	350-600°C under N_2 for 5 h	Glass (heated by an infrared lamp)	300 Å -3000 Å	34
γ-Fe_2O_3	Iron(III) nitrate (+boric acid) +ethylene glycol	T=80 °C under N_2 Iron nitrate 28 wt% μ= ~ 80cp	200°C in air	300-550°C under vacuum *better 450°C	Glass	0.1-0.2 μm	35
α-Fe_2O_3 Fe_3O_4 γ-Fe_2O_3	Iron(III) nitrate + 2-methoxyethanol +2,4 pentanedione	T=30 °C for 2 h 1:20:2 molar ratio	Prior heating 800 °C, 10 min	1. (α-Fe_2O_3) 2. 600°C 5 h under N_2 (Fe_3O_4) 3. 400°C 5 h under air (γ-Fe_2O_3)	SiO_2 glass	-	36
α-Fe_2O_3	Iron(III) nitrate +2-methoxyethanol +acetylacetone	Stirring at RT for 2 h iron nitrate 0.2-0.5 M (best results 0.3 M)	1 h at 300, 400 and 500 °C rate 100 °C /h	124 °C	Glass	50 nm	37
α-Fe_2O_3	Ferric nitrate +ferrous sulfide +ammonium hydroxide	-	100 °C 15 min	150-500°C	Glass	-	38

Table 2.3. (Continued) The literature survey of the sol-gel processes which were used to produce maghemite, hematite and magnetite thin films.

Formed phases	**Solvent and precursor**	**Experiment details**	**Drying time and temperature**	**Annealing time and temperature**	**Substrate**	**One-layer thickness**	**Ref. no**
α-Fe_2O_3	Iron(III) nitrate + 2-methoxyethanol	50 °C in N_2 atm	350 °C	400-700 °C for 3 h	Quartz for UV-VIS; Si [111] for XRD	0.5 μm	39
Fe_3O_4	$FeCl_2.4H_2O$ + citric acid monohydrate + antioxidant agent + ethanol absolute	Stirred at 60 °C 6 h	100°C	250–400 °C for half an hour	Silica glass	0.1 mm	40
Fe_3O_4	Iron(II) lactate +Iron(III) nitrate + ethylene glycol +citric acid monohydrate + ethanol	10 h stirring	40°C for 1 h	450 °C for 3 h under N_2	Quartz	120-275 nm	41
Fe_3O_4	Iron (III) nitrate +2-methoxyethanol +polyethylene glycol	Stirring= 70°C μ= ~ 13 mPas	100 °C for 10 min	350 °C under N_2 Rate 3 K/min.	Fused quartz	0.3 μm	42

2.4.2. Spin Coating Process

Sol-gel is one of the simplest and most common techniques of applying thin films onto substrates. The material to be made into the coating must be dissolved or dispersed into a solvent of some kind, and this coating solution is then deposited onto the surface and spun-off to leave a uniform layer for subsequent processing stages and ultimate use [43].

Four distinct stages to the spin coating process are shown on Figure 2.6. Stage 3 (flow controlled) and stage 4 (evaporation controlled) are the two stages that have the most impact on final coating thickness.

The first stage is the deposition of the coating fluid onto the substrate. It can be done using a nozzle that pours the solution out or it could be sprayed onto the surface, etc. Usually this dispense stage provides a substantial excess of coating solution compared to the amount that will ultimately be required in the final coating thickness. For many solutions it is often beneficial to dispense through a sub-micron sized filter to eliminate particles that could lead to flaws. Another potentially important issue is whether the solution wets the surface completely during the dispense stage. If not, then incomplete coverage can result.

The second stage is when the substrate is accelerated up to its final desired rotation speed. This stage is usually characterized by aggressive fluid expulsion from the substrate surface by the rotational motion. Because of initial depth of fluid on the substrate surface, spiral vortices may briefly be present during this stage; these would form as a result of the twisting motion caused by the inertia that the top of the fluid layer exerts while the substrate below rotates faster and faster. Eventually, the fluid is thin enough to be completely co-rotating with the substrate and any evidence of fluid thickness differences is gone. Ultimately, the substrate reaches its desired speed, and the fluid is thin enough that the viscous shear drag exactly balances the rotational accelerations.

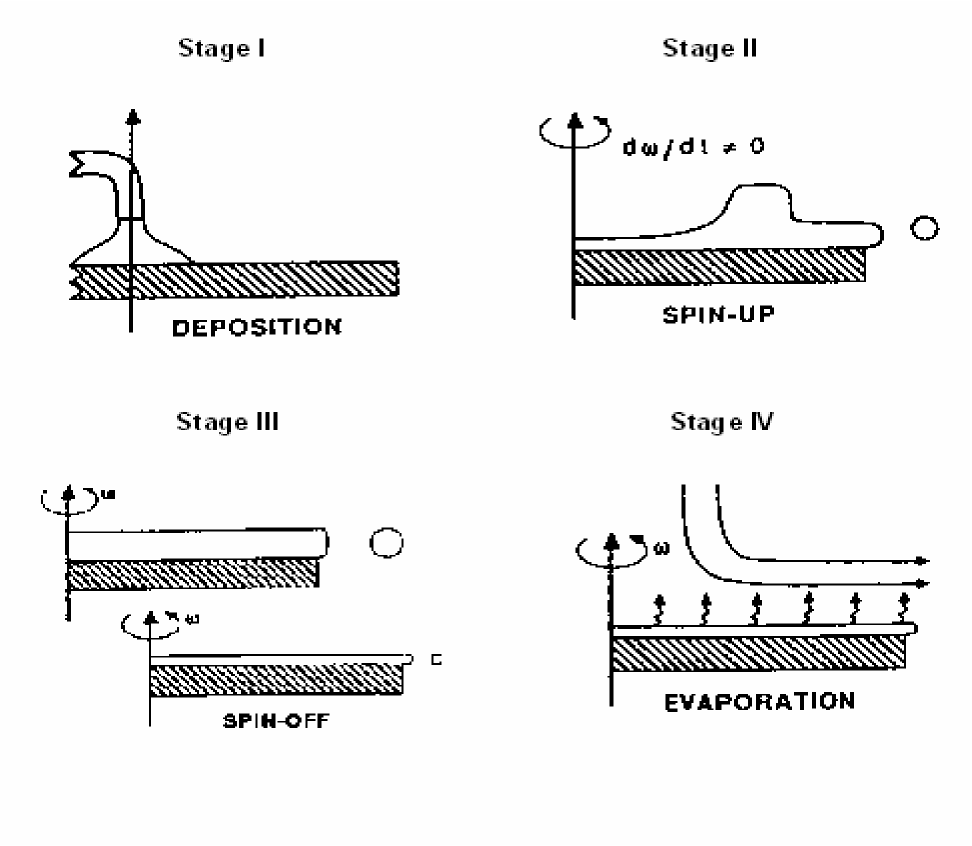

Figure 2.6. Stages of the spin coating process [44].

The third stage is when the substrate is spinning at a constant rate and fluid viscous forces dominate fluid thinning behavior. This stage is characterized by gradual fluid thinning. Fluid thinning is generally quite uniform, though with solutions containing volatile solvents; it is often possible to see interference colors "spinning off", and doing so progressively more slowly as the coating thickness is reduced. Edge effects are often seen because the fluid flows uniformly outward, but must form droplets at the edge to be flung off. Thus, depending on the surface tension, viscosity, rotation rate, etc., there may be a small bead of coating thickness difference around the rim of the final substrate.

The fourth stage is when the substrate is spinning at a constant rate and solvent evaporation dominates the coating thinning behavior. As the prior stage advances, the fluid thickness reaches a point where the viscosity effects yield only rather minor net fluid flow. At this point, the evaporation of any volatile solvent species will become the dominant process occurring in the coating. In fact, at this point the coating effectively “gels” because as these solvents are removed the viscosity of the remaining solution will likely rise.

The prediction of Mayerhofer about factors affecting the film thickness (*t*) includes the spin rate (f), the initial viscosity (η_i), and the evaporation rate (e) [43]:

$$t \ \alpha \ f^{2/3}\eta_i^{1/3}e^{1/3} \qquad \text{Eq. [2.7]}$$

It can be easily seen from the equation that viscosity and spinning rate has inseparable affect on thin film formation. To understand the behavior of the solution during spin coating step, viscosity properties should also be investigated.

2.4.2.1. Viscosity

Viscosity is a measure of the resistance of a fluid to deform under shear stress. Viscosity describes a fluid's internal resistance to flow and may be thought of as a measure of fluid friction.

For straight, parallel and uniform flow, the shear stress, τ, between layers is proportional to the velocity gradient, $\partial u / \partial y$, in the direction perpendicular to the layers, in other words, the relative motion of the layers.

$$\tau = \mu \frac{\partial u}{\partial y} \qquad \text{Eq. [2.8]}$$

where the constant μ is known as the coefficient of viscosity, the viscosity, or the dynamic viscosity. Many fluids satisfy Newton's criterion and are known as

Newtonian fluids. Non-Newtonian fluids exhibit a more complicated relationship between shear stress and velocity gradient than simple linearity.

Newtonian and non-Newtonian behaviours of fluids are given in Figure 2.7. When the viscosity decreases with increasing shear rate, it is called the fluid shear-thinning. In opposite case where the viscosity increases as fluid is subjected to a higher shear rate, fluid is called shear-thickening [45].

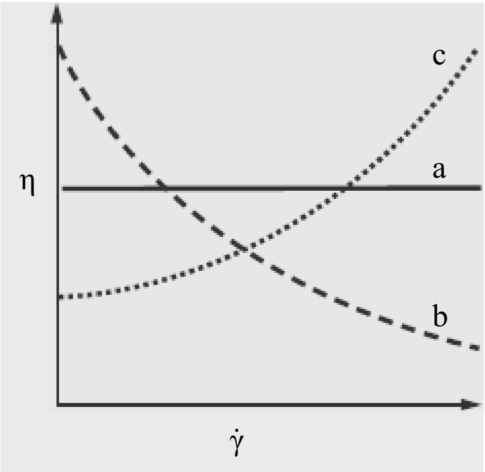

Figure 2.7. (a) Newtonian, (b) shear thinning and (c) shear thickening non Newtonian behaviors [45].

The regions where the apparent viscosity is approximately constant are known as Newtonian regions. The behavior between these regions can usually be approximated by a straight line on these axes. It is known as the power-law region. In this region, the behavior can be approximated by

$$\log \eta = a + b \log \dot{\gamma} \qquad \text{Eq. [2.9]}$$

where η is viscosity, $\dot{\gamma}$ is shear rate, *a* is the intersect of the curve and *b* is the slope of the curve, which were shown in Figure 2.9. It can be rewritten as

$$\eta = K\dot{\gamma}^{b} \qquad \text{Eq. [2.10]}$$

where $K = \exp(a)$. Instead of *b*, *(n-1)* is commonly used for the exponent and write result for the apparent viscosity as follows.

$$\eta = K\dot{\gamma}^{n-1} \qquad \text{Eq. [2.11]}$$

Upon using the connection among the shear stress, apparent viscosity, and the shear rate the power-law model is obtained.

$$\tau = K\dot{\gamma}^{n} \qquad \text{Eq.[2.12]}$$

where *n* is called the power-law index. It is an important fact that *n* =1 corresponds to Newtonian behavior. Typically, for shear thinning fluids, it lies between 1/3 and, 1/2 and for shear thickening fluids it is higher than 2 [45]. Solutions having power law index near 1 (between 1.1- 0.9) can be accepted as Newtonian behavior.

It is well known that non uniform films are expected from spinning non-Newtonian fluids [46, 47]. Non-Newtonian solutions change their viscosities depending on what shear rate is used, thus depending on distance from the center, the shear rate will be different and thus the flow behaviour. This can give radial thickness variation that varies rather smoothly in a radial sense [46].

2.4.3. Drying and Annealing of Maghemite Thin Films

After preparation of the sol-gel solution, heating treatment of the deposited film is the final step for the formation of maghemite thin films.

First stage for the thin film production from the sol-gel solution is the drying step by which water and solvent in the solution are removed. There are some stages occurring during drying process. In the first stage called constant rate period, liquid flows to the surface to replace that which is lost to evaporation. This is the stage where the most shrinkage and warping occur as a result of capillary pressure differentials within the film. The gel matrix reaches a point called critical point where it can no longer shrink to release the solvent necessary to reduce the capillary pressure. At this point the liquid meniscus enters the matrix and drying from within the film begins. This is when a crack is the most likely to appear in the material. In the first falling rate period, the last layers of solvent are removed by flow along the pores walls to the surface. During second falling rate period, the volatized solvent is removed by the diffusion of vapor to the surface.

The timing of these stages is intimately linked to the structure of the film. Cracking is the most important subject that should be considered during the drying. The gel consists of two phases, the network solid phase and connected pores filled with liquid phase. Initially the surface of the gel is covered with liquid phase. The liquid phase evaporates so that the solid phase is exposed. Since the solid network is wetted by the liquid phase, the liquid phase tends to cover all the solid surface capillary force will be imposed on the solid network. Since the gel network is compliant, the gel shrinks under capillary force as the liquid evaporates [32].

The annealing process changes the organic precursor film into an inorganic ceramic film by the pyrolysis of organometallic compounds. During this process, the lead acetate dehydrates, melts and decomposes. In this stage, the dried film becomes wet again and the organic compounds begin to decompose. The internal stress is relaxed and the volume change of the film continues [43]. At the end of this stage, the organic film changes to iron oxide film. At higher temperatures, maghemite transforms to hematite which is the more stable phase [48].

CHAPTER 3

EXPERIMENTAL PROCEDURE

In this study, maghemite thin films were prepared by spin-coating an iron nitrate containing solution on glass and quartz substrates. The film thickness was adjusted by changing the spinning rate of the spin coater. In order to examine the effect of the thickness of the films, individual layer coating steps were repeated. To form maghemite phase containing thin films, annealing was carried out at several temperatures for different time periods. The solution properties were investigated by viscosity measurements, TG (Thermogravimetry) and DTA (Differential Thermal Analysis). The films were characterized by XRD, TEM, SEM, UV-VIS and VSM.

3.1. Solution Preparation

In this study, iron (III) nitrate [$Fe(NO_3)_3.9H_2O$] was used as the precursor and dissolved in a mixture of 2-methoxyethanol and acetylacetone in a molar ratio of 20:2. Molar ratio of iron (III) nitrate kept as 0.3 M in the solution. Then the mixture was stirred at room temperature for 2 hours [51]. During stirring, iron nitrate was dissolved in the solvent. All thin films were prepared by using this solution and for convenience, this solution was called as S1. Flow diagram for the preparation of S1 solution is shown on Figure 3.1.

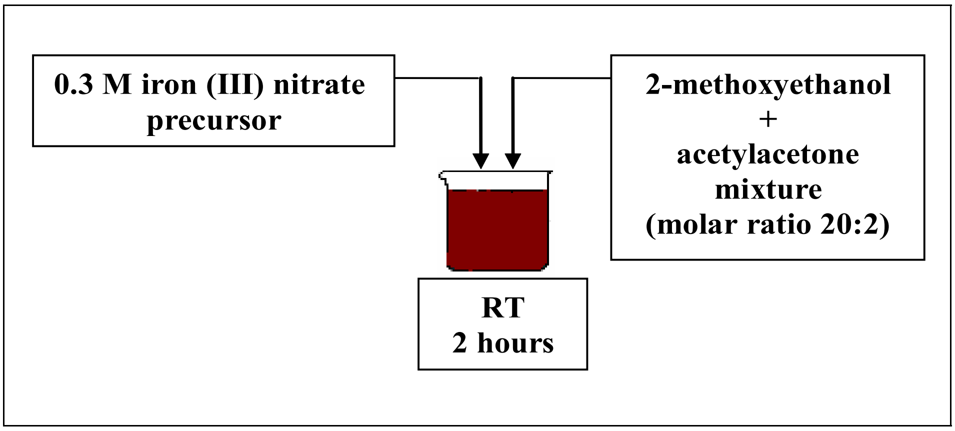

Figure 3.1. The flow diagram of solution preparation used for the production of maghemite thin films.

It is observed in the literature that the films which were obtained using iron (III) nitrate shows a higher maghemite to hematite transformation temperature compared to the films produced by using iron chloride precursors [37]. Therefore, iron (III) nitrate was selected as the starting precursor in this thesis.

In order to investigate the solution properties, two other preparation routes were followed. For both solutions, iron (III) nitrate was used as the precursor. Second solution, which was called as S2, was prepared by using iron (III) nitrate and 2-methoxyethanol. 15 wt% iron (III) nitrate solution was prepared and then stirred at 80 °C for 1 hour.

In the third solution, which was called as S3, iron (III) nitrate was dissolved in ethylene glycol. The concentration of iron nitrate in ethylene glycol was 28 wt% in this solution. Mixture was stirred at 80 °C for 1 hour [35]. The solution preparation steps were summarized in Table 3.1.

Table 3.1. Precursors and solvents used in this study.

Solution	**Precursor**	**Solvent(s)**	**Stirring Temperature**	**Stirring Time**
S1	Iron Nitrate (0.3 M)	2-methoxyethanol acetylacetone (20:2)	RT	2 hours
S2	Iron Nitrate (15 wt%)	2-methoxyethanol	80 °C	1 hour
S3	Iron Nitrate (28 wt%)	Ethylene glycol	80 °C	1 hour

For the preparation of maghemite thin films, 4.32 grams of iron (III) nitrate was dissolved in 30.42 grams of 2-methoxyethanol and 4 grams of acetylacetone. The mixture (S1) was stirred for 2 hours at room temperature. For the second solution (S2), 3.75 grams of iron (III) nitrate was added to 21.25 grams of 2-methoxyethanol. Then they were stirred at 80 °C for 1 hour. For the third solution (S3), 7 grams of iron (III) nitrate and 18 grams of ethylene glycol were mixed and they were stirred at 80 °C for 1 hour like the second solution.

In this study, only the first solution which was called as S1 was used to prepare maghemite thin films. Other solutions were prepared in order to compare the effect of the solvent and iron (III) nitrate concentration on maghemite formation.

3.2. Preparation of Maghemite Thin Films

3.2.1. Preparation of Substrates

The preparation of maghemite thin films with homogeneous and crack-free surfaces is one of the aims in this study. In many cases, the observation of physical and chemical properties such as adsorption, diffusion, oxidation or reduction requires the use of films with smooth surfaces. In the same way magnetic, electronic or optical attributes of thin films are dependent on the homogeneity of the individual layers, as well as on the roughness of the boundaries between the layers. In general, the surface and volume microstructures of thin films depend strongly on all the details of the coating process such as the substrate and the thin film material, the substrate surface and the experimental conditions.

Glass and quartz were used as substrates for maghemite thin films although alumina and pure silica were also tried. Glass is easy to work with as it etches quickly, can be coated at relatively low temperatures, and is inexpensive. Other substrate used during the study was quartz. During the experiment it was observed that quartz substrates behave like glass substrates. Unfortunately, quartz is difficult to work with as the etching rate is slow and the cost of quartz substrates can be almost 2-3 fold higher than glass substrates. Before cleaning, substrates were cut to the desired dimensions. The dimensions of the glass substrates are different for different characterization techniques such as for SEM 0.5 x 0.5 cm^2 substrates were used. On the other hand, for parallel beam X-Ray diffraction method more than 2.5 x 1.5 cm^2 dimensions are required.

Thin film growth and adhesion are fundamentally related to the substrate surface conditions. Therefore it is crucial to clean the substrate thoroughly before the deposition process. Two methods were used to clean the surface throughout the study. These methods were ultrasonic cleaning and piranha solution etching.

In ultrasonic cleaning, the substrate was rinsed in acetone and cleaned by using an ultrasonic system for 15 minutes. The second method, which is surface etching with piranha solution, was used to get more active surface. Surface etching method is more complex and it takes longer time than the ultrasonic cleaning method. In this method, substrates were rinsed with 1 % detergent solution and cleaned in an ultrasonic bath for 15 minutes. After cleaning the substrates with deionized water, substrates were immersed into piranha solution for 24 hours. Piranha solution was prepared with a volume ratio of 1:5, H_2O_2 (hydrogen peroxide) and H_2SO_4 (sulphuric acid). After 24 hours, the substrates were washed carefully with deionized water. The final step was the ultrasonic cleaning procedure. The substrate preparation steps were given in Figure 3.2.

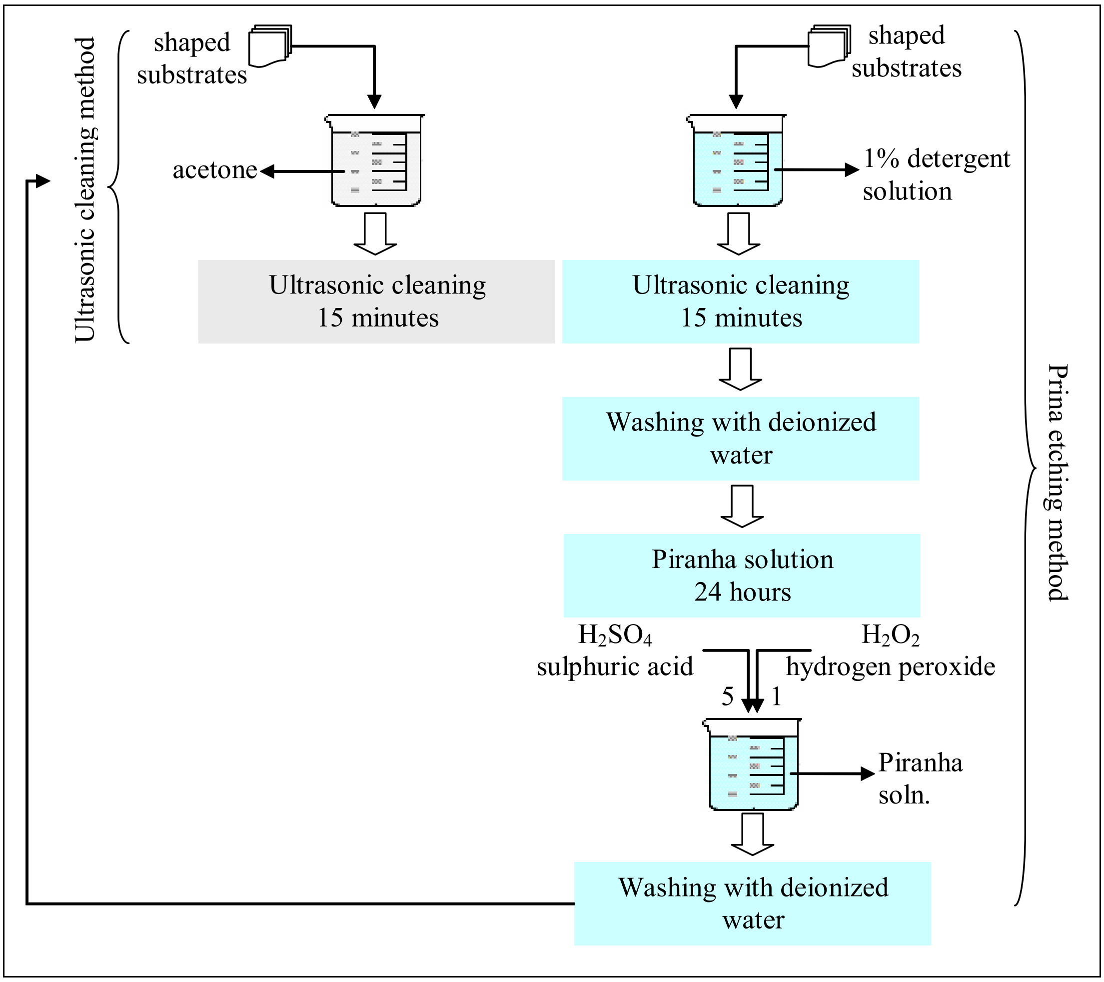

Figure 3.2. Routes for substrate preparation.

3.2.1.1 Piranha solution

Piranha is a trade name for a chemical mixture consisting of sulphuric acid (H_2SO_4) and hydrogen peroxide (H_2O_2). Because the mixture is a strong oxidizer, it will remove most organic matter, and it will also hydroxylate most surfaces, making them extremely hydrophilic. Many different mixture ratios are commonly used and they are all called as piranha [52].

There are two main applications for piranha solution. Firstly, it is used to remove organic contaminants from the surface of the substrate during cleaning sequences. Secondly, it is used to strip photoresist from the surface of the substrate.

The effectiveness of piranha solution in removing organic residues is due to two distinct processes that operate at noticeably different rates. The first and faster process is the removal of hydrogen and oxygen as units of water by the concentrated sulphuric acid. This occurs because hydration of concentrated sulphuric acid is thermodynamically strongly favorable, with a ΔH of -880 kJ/mol. It is this rapid dehydrating property, rather than acidity itself, that makes both concentrated sulphuric acid, and so piranha solution, very dangerous to handle.

The dehydration process exhibits itself as the rapid carbonisation of common organic materials, especially carbohydrates, when immersed in piranha solution. Piranha solution was named in part for the vigour of this first process, since large quantities of organic residues immersed piranha solution are dehydrated so violently that the process resembles a piranha feeding frenzy. The second and more definitive rationale for the name, however, is the ability of piranha solution to "eat anything," including in particular elemental carbon in the form of soot or char.

This second and far more interesting process can be understood as the sulphuric-acid boosted conversion of hydrogen peroxide from a relatively mild oxidizing agent to dissolve elemental carbon, a material that is notoriously resistant to room temperature aqueous reactions. This transformation can be viewed as the energetically favourable dehydration of hydrogen peroxide to form hydronium ions, bisulfate ions, and, transiently, atomic oxygen.

$$H_2SO_4 + H_2O_2 \longrightarrow H_3O^+ + HSO_{4^-} + O \qquad \text{Eq. [3.1]}$$

It is this extremely reactive atomic oxygen species that allows piranha solution to dissolve elemental carbon. Carbon allotropes are difficult to attack chemically because of the highly stable and typically graphite-like hybridized bonds that surface carbon atoms tend to form with each other. The most likely route by which piranha solution disrupts these stable carbon-to-carbon surface bonds is for an atomic oxygen first to attach directly to a surface carbon to form a carbonyl group.

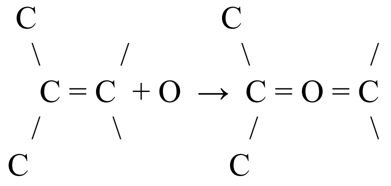

Eq. [3.2]

In the above process, the oxygen atom in effect "steals" an electron bonding pair from the central carbon, forming the carbonyl group and simultaneously disrupting the bonds of the target carbon atom with one or more of its neighbours. The result is a cascading effect in which a single atomic oxygen reaction initiates significant "unraveling" of the local bonding structure, which in turn allows a wide range of aqueous reactions to affect previously impervious carbon atoms. Further oxidation, for example, can convert the initial carbonyl group into carbon dioxide and create a new carbonyl group on the neighbouring carbon whose bonds were disrupted.

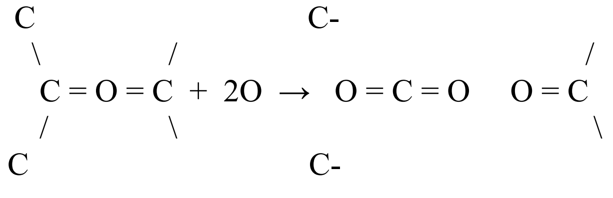

Eq. [3.3]

The carbon removed by piranha solution may be either original residues or char from the dehydration step. The oxidation process is slower than the dehydration process, taking place over a period of minutes. The oxidation of carbon exhibits itself as a gradual clearing of suspended soot and carbon char left by the initial dehydration process. In time, piranha solutions in which organic materials have been immersed typically will return to complete clarity, with no visible traces of the original organic materials remaining.

A final minor contribution to the piranha solution cleaning is its high acidity, which dissolves deposits such as metal oxides and carbonates. However, since it is safer and easier to remove such deposits using milder acids, piranha solution is more typically used in situations where high acidity complicates cleaning instead of assisting it. For substrates with low tolerance for acidity, the alkaline oxidising solution known as base piranha can be used instead [52].

3.2.2. Spin Coating

The spin coating process was performed by Chemat Technology Spin Coater. After solution preparation, spin coating was performed onto glass and quartz substrates. After cleaning small substrates pieces, they were stuck on the head of the spin coater with the help of a double-sided tape. Excess amount of solution was poured onto the substrate using pasteur pipette.

The film thickness was adjusted by changing the spinning rate of the spin coater. In this study, films were coated at 1400 and 4000 rpm for 1 minute. For the production of crack free films, very thin films were produced. In order to examine the effect of the thickness of the films, individual layer coating steps were repeated.

3.2.3. Heat Treatment of Maghemite Thin Films

The heat treatment of the maghemite thin films was begun with the drying process. Drying temperature was determined according to solvent melting temperature. Drying temperature in the experiments was decided as 110 °C since the boiling points of the organic solvents in the solution S1 were 124 °C and 139 °C for 2-methoxyethanol and acetylacetone, respectively.

Because of the shrinkage taking place during removal of water, drying process is important. For the removal of water, the specimens were fired at 110 °C for 15 minutes in the preheated furnace. Drying step was performed in between each layer. These steps were repeated until the desired thickness was obtained. Figure 3.3 shows the route that was followed starting from the solution preparation step to heat treatment processes.

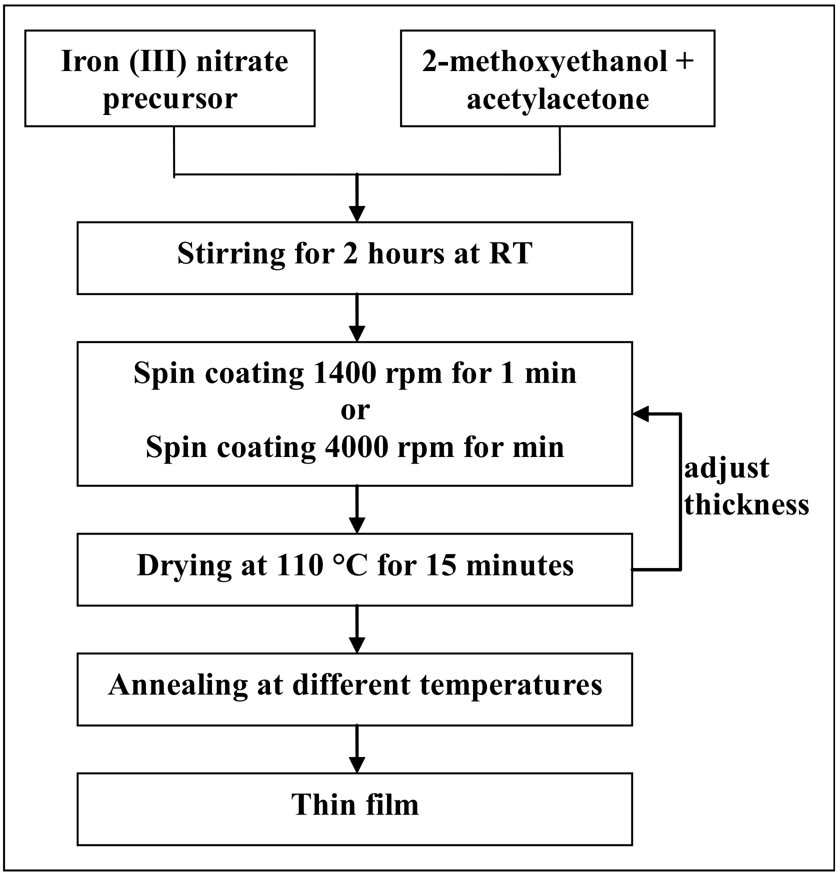

Figure 3.3. The flow chart for the production of thin films

Final heat treatment step for the thin films is annealing. Annealing process was preformed in a conventional furnace with the heating rate of 2 °C/min. Since it was observed that maghemite formation favoured by fast cooling [48], the samples were taken outside the furnace as soon as annealing step was completed.

Annealing of the thin films, in terms of its temperature and time, plays an important role in the maghemite formation and stabilization. Because of the fact that maghemite easily transforms to hematite with increasing annealing temperature and time, annealing becomes the key factor for this study.

To understand the effect of temperature, five distinct temperatures 300 °C, 350 °C, 400 °C, 500 °C and 600 °C were selected. Duration of the annealing process was determined as 1 hour, 2 hours and 4 hours.

The effect of the film thickness on maghemite formation was also investigated. Several different thicknesses were examined. Thickness of one layer was determined by controlling the spinning rate. Thin films consisting of one layer to twenty layers were investigated to understand the effect of the thickness on the maghemite to hematite transition temperature.

The experimental parameters which are annealing temperature, annealing time and sample thickness should not be evaluated individually. They are all connected to each other. For instance, during evaluation of the thickness effect on maghemite thin films, it should be known that the layers of maghemite, in the multi-layered films, are subjected to a total thermal treatment time longer than that of the single layered films. In this study, although the effects of each parameter were examined separately, the relation between them should be taken into consideration.

3.3. Characterization of Solutions

Characterization of the maghemite thin films is important to understand and optimize the maghemite to hematite transition and to obtain totally maghemite phase containing thin films. To be able to obtain such films containing only maghemite, solution properties were also investigated.

3.3.1. Viscosity

Viscosity of the solution S1 was measured by Dynisco, LCR-7001 model capillary Rheometer. Viscosity is an important parameter for thin films because homogeneity of the film is determined by the viscosity and applied strain rate relation.

3.3.2. TGA/DTA

The differential thermal analysis (DTA) is a thermal technique in which the heat effects, associated with physical or chemical changes, are recorded as a function of temperature and time as the substance is heated at a uniform rate. Heat or enthalpic changes, either exothermic or endothermic, are caused by phase transitions, such as crystalline structure inversions, dehydration reactions, dissociation reactions or decomposition reactions and chemical reactions. Generally speaking, phase transitions, dehydration, reduction, and some decomposition reactions produce endothermic effects; whereas crystallization, oxidation, and some decomposition reactions produce exothermic effects [48].

TG (thermogravimetry) and DTA (differential thermal analysis) analysis were conducted by Simultaneous Thermogravimetric Analyser and Differential Thermal Analyser (SETARAM) in Central Laboratory at METU. For these analyses, solution S1 was dried at 100 °C for 8 hours in the low temperature furnace to obtain a gel powder. TG/DTA analyses were done from room temperature up to 980 °C with a heating rate of 3 °C/min.

3.4. Characterization of Maghemite Thin Films

3.4.1. Structural and Morphological Analysis

X-Ray diffraction (XRD) analyses were performed by using Rigaku D/MAX 2200/PC (Japan) diffractometer. Two different methods were used for XRD analysis. The first method was Bragg-Brentano parafocusing method which is the traditional method for the characterization of powders and bulk samples. This method was used for most of the samples between angles 10°-70° (2θ) with CuK_α (λ=0.15418) radiation (40 kV/40 mA). The scanning rate for focusing method was determined as 2°/minute. Bragg-Brentano parafocusing method of x-ray characterization yielded not only the information about the structure of the samples but also the information about the particle size of powder samples obtained from the different solutions, namely S1, S2 and S3, used in the study. The average particle sizes of the samples were estimated by Scherrer's formula.

Second method, which is parallel beam method, was used to decrease the effect of the substrates in some of the samples. The schematic diagram of parallel beam method is given in Figure 3.4. In this Figure DS is the divergence slit, SS is the scatter slit and RS is the receiving slit.

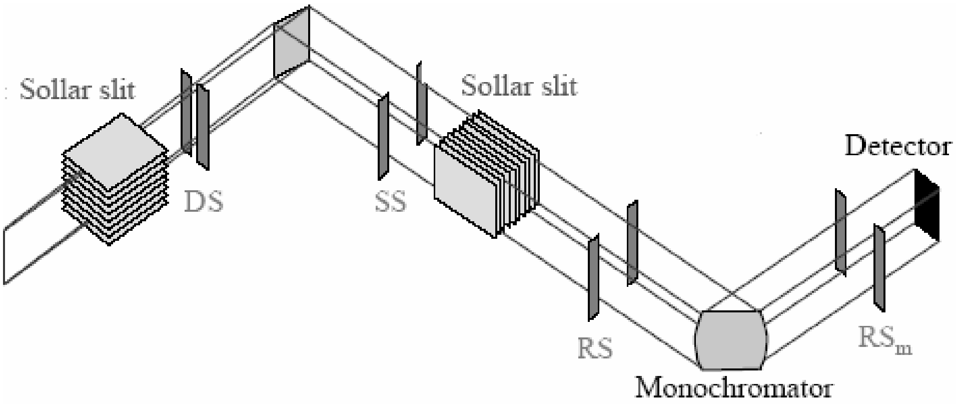

Figure 3.4. The schemetic diagram of parallel beam method.

The focusing method has been extensively used in powder diffractometry. However, this method is sensitive to the sample displacement error and flatness of the sample. As a result, systematic errors commonly occurred. Parallel beam method on the contrary, gives precise peak positions, which is unaffected by sample displacement. This is crucial for thin film characterization. In this process only requirement is suitable sample area. Slit width and incidence angle are chosen according to sample dimensions. All calculations were made by using simple geometrical facts. The distances and detailed information about equipment of the x-ray device are given in Figure 3.5.

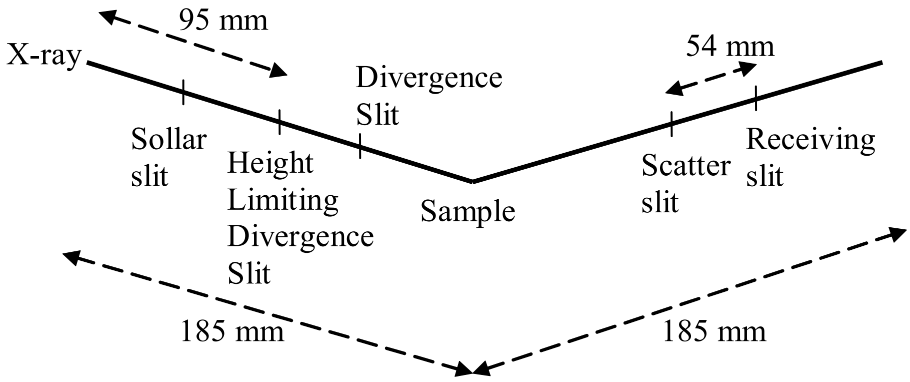

Figure 3.5. The schematic diagram of the x-ray equipment.

For instance, the length of the sample was determined by using distance relation between the height limiting divergence slit and the sample. The distance between the x-ray source and the sample holder slit is 185 mm and the distance between the x-ray source and the height limiting divergence slit is 95 mm. If the height limiting divergence slit is chosen as 5 mm type, which means the distance between the two parts of the height limiting divergence slit, geometrically the length of the sample is calculated according to equation [3.4].

$$\frac{X}{185}=\frac{5}{95} \qquad \text{Eq. [3.4]}$$

The length of the sample has to be larger than 9.7 mm if the height limiting divergence slit is chosen as 5 mm slit. The height limiting divergence slits can be chosen as 1.2, 2, 5 and 10 mm according to the sample lengths.

For the width calculations of the sample, relation between the slit width and incidence angle should be evaluated. In Figure 3.6 the relation of the sample dimensions, slit width and incidence angle can be seen.

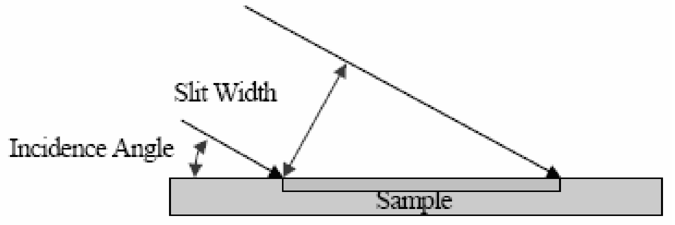

Figure 3.6. The schematic view of the measurement conditions of the parallel beam method.

The relation between slit width and incidence angle is given in equation [3.5].

$$\frac{Slit\ Width}{Sample\ Width}=\mathrm{Sin}\ \ (Incidence\ Angle) \qquad \text{Eq. [3.5]}$$

By choosing proper divergence slit (slit width) and incidence angle, which are directly entered to the software, the required minimum width of the sample can be found. It should be mentioned that with increasing incidence angle, the effect of the substrate increases but the required width sample decreases. Moreover, divergence slit directly affects the intensity of the x-ray data.

Electron diffraction studies were done by using a JEOL JEM 3010 Transmission Electron Microscopy (TEM) at Kırıkkale University. Furthermore, chemical and surface topography analyses of maghemite thin films were carried out by JEOL JSM-6400 Scanning Electron Microscope (SEM) equipped with an Energy Dispersive Spectrometer (EDS) and ZEISS-SUPRA 50 VP Field Emission Scanning Electron Microscope (FE-SEM) at Anadolu University.

3.4.2. Optical Analysis

Optical transmittance of the films was measured by SHIMADZU 160 UV-VIS Spectrometer in the Department of Chemistry at METU. Transmittance (%)-Wavelength (nm) curves (optical transmission spectrum) were drawn in the range of 300 nm - 800 nm and optical properties such as absorption coefficient (α) and extinction coefficient (k) of the thin films were obtained. Modified envelope method was used to find the optical properties of thin films annealed at 500º C as given in Chapter 4.

3.4.2.1. Modified Envelope Method

The modified envelope method, which includes the consideration of the light intensity loss from the back surface of the substrate, was developed and shown to be a simple and convenient tool for obtaining the optical properties and the thickness of the film by using the transmission spectra alone in the medium and weak absorption regions. In the near-optical band gap region, both the transmission and reflection spectra were used to calculate the optical constants of the films.

In a multi layer thin-film system, if the complex refractive index and thickness of each film layer are known, the reflectance (R) and transmittance (T) can be calculated exactly no matter how many layers are in the system or what the incident angle of the light is. All these quantities except the film thickness are wavelength-dependent. However, in practice, a reverse calculation is needed, i.e., the optical constants and thickness of the film (d) need to be calculated from the measured reflection and transmission spectra. There are only two measurable reflection and transmission spectra. There are only two measurable quantities, T and R, but 3m+2 unknowns (three unknowns, n,k, and d, for each layer of m layer films and two unknowns, n and k, for the substrate) at a given wavelength and an incident angle. For a simple thin film system consisting of a single film on a substrate, there are still three unknowns for the film but two measured, T and R, for a given wavelength and an incident angle, assuming the optical constants of the substrate are known. The difficulty of calculating the optical constants and the thickness of the film from T and R is not only that the number of unknowns is larger than the number of quantities one can measure, but also that the optical constants cannot be explicitly expressed in terms of T and R.

Fortunately, for a single layer weakly absorbing film on a transparent substrate, the refractive index and extinction coefficient as a function of wavelength and film thickness can be obtained from the transmission spectra alone. This method, which is referred to hereafter as the envelope method, was first presented by Manifacier et al. This is a very useful approach to study the optical properties of insulating films, since most of them are weakly absorbing materials [53].

Figure 3.7 shows the schematic diagram of a weakly absorbing thin film on a completely transparent substrate. Note that, for the original envelope method, the substrate is considered as semiinfinite. The refractive index of the ambient is n_0; n_s is the refractive index of the substrate; n, k, and d denote the refractive index, extinction coefficient, and the thickness of the film, respectively.

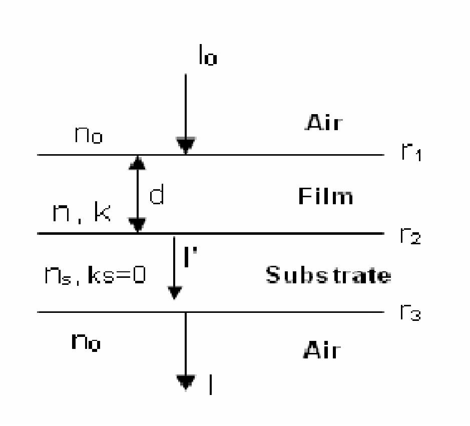

Figure 3.7. Schematic diagram of the modified envelope method: a weakly absorbing thin film on a completely transparent finite substrate [53].

$$T = I / I_0 = (1 - r_3) I^{'} / I_0 \qquad \text{Eq. [3.6]}$$

The transmittance ($T^{'}$) of a single film on a transparent semi-infinite substrate can be expressed as:

$$T^{'} = \frac{Ax}{B - Cx - Dx^2} \qquad \text{Eq. [3.7]}$$

where $x = \exp(-\alpha d)$, Eq. [3.8]

$A = 16 n_0 n_s (n^2 + k^2)$,

$B = [(n_0 + n)^2 + k^2][(n + n_s)^2 + k^2]$,

$C = 2\ [(n^2 - n_0{}^2 + k^2)(n^2 - n_s{}^2 + k^2) - 4k^2 n_s]\cos(\gamma) - 2\ [2kn_s(n^2 - n_0{}^2 + k^2) + 2k(n^2 - n_s{}^2 + k^2)]\sin(\gamma)$,

$D = [(n - n_0)^2 + k^2][(n - n_s)^2 + k^2]$, α is the absorption coefficient of the film which is equal to $4\pi k/\lambda$, γ is equal to $4\pi nd/\lambda$, d is the film thickness, k is the extinction coefficient of the film, and n_0, n, and n_s are the refractive indices of the ambient (air), film, and substrate, respectively. Equation [3.7] is valid only if the film is homogeneous, the thickness of the film is uniform, and the substrate is semi infinite and completely transparent, i.e. $k_s = 0$.

The equations describing the envelope method can be derived from Eq. [3.7] with further assumptions where the square of the refractive index of the film is much greater than that of extinction of the film, i.e., n^2 » k^2, and the square of the refractive index difference between the film and air and the film and the substrate is much greater than that of the extinction coefficient of the film, i.e., $(n-1)^2 \gg k^2$ and $(n-n_s)^2 \gg k^2$. The first assumption leads to $A = 16n_0n^2n_s$, and $B=(n_0+n)^2(n+n_s)^2$.

The second assumption leads to $C = [(n^2-n_0{}^2)(n^2-n_s{}^2)]\cos(\gamma)$ and $D=(n-n_0)^2(n-n_s)^2$ .With the above assumptions, equation [3.7] becomes

$$T' = \frac{16n_sn^2x}{(1+n)^2(n+n_s)^2 - 2x[(n^2-1)(n^2-n_s{}^2)]\cos(\gamma) + (n-1)^2(n-n_s)^2x^2} \qquad \text{Eq. [3.9]}$$

Here 1 is used to replace n_0, which is refractive index of air, and $\gamma = 4\pi nd/\lambda$. The cosine function in the denominator oscillates between +1 and -1, which results in the well-known equation for the interference fringes in the transmission spectrum:

$$2nd = m\lambda \qquad \text{Eq. [3.10]}$$

where the order number m is an integer for maxima and a half-integer for minima. Equation [3.10] gives the top envelope equation for cos (γ) =1 as

$$T'_{\max} = \frac{16n_s n^2 x}{[(1+n)(n+n_s)-(n-1)(n-n_s)x]^2} \qquad \text{Eq. [3.11]}$$

Whereas, for cos (γ) = -1, the bottom envelope equation becomes

$$T'_{\min} = \frac{16n_s n^2 x}{[(1+n)(n+n_s)+(n-1)(n-n_s)x]^2} \qquad \text{Eq. [3.12]}$$

T_{min} and T_{max} as continuous functions of λ through n(λ) and α(λ). These functions are the envelopes of the maxima $T_{max}(\lambda)$ and the minima $T_{min}(\lambda)$ in the transmission spectrum.

Equations [3.11] and [3.12] can be solved for n and x, giving

$$x = \frac{(n+1)(n+n_s)[(T'_{\max}/T'_{\min})^{0.5}-1]}{(n-1)(n-n_s)[(T'_{\max}/T'_{\min})^{0.5}+1]} \qquad \text{Eq. [3.13]}$$

$$n = [N' + (N'^2 - n_s{}^2)^{0.5}]^{0.5} \qquad \text{Eq. [3.14]}$$

where $$N' = \frac{1}{2}(1+n_s{}^2) + 2n_s(T'_{\max} - T'_{\min})/(T'_{\max}T'_{\min}) \qquad \text{Eq. [3.15]}$$

The thickness t of the layer can be calculated from two maxima or minima [54]:

$$t = \frac{M\lambda_1\lambda_2}{2(n(\lambda_1)\lambda_2 - n(\lambda_2)\lambda_1)} \qquad \text{Eq. [3.16]}$$

where *M* is the number of oscillations between the two extrema (*M*= 1 between two consecutive maxima or minima); λ_1, $n(\lambda_1)$ and λ_2 through $n(\lambda_2)$ are the corresponding wavelengths and indices of refraction.

3.4.3. Magnetic Analysis

VSM measurements were done by using Lake Shore Model 7407 Vibrating Sample Magnetometer. Hysteresis M-H curves were recorded at ambient temperature. These measurements were conducted on specimens having approximately 10x10 mm^2 surface areas and the results were presented in terms of emu, mass magnetization in cgs-units, i.e., emu/g and in emu/cm^3.

CHAPTER 4

RESULTS AND DISCUSSION

In this study, basic aim was to produce maghemite thin films and investigate the experimental parameters to obtain this maghemite phase in the films. These parameters are annealing temperature, annealing time and thickness of the thin films. Preparation of stable solutions played an important role on the production of homogeneous and crack free films. Solution properties were investigated by TGA (Thermogravimetry), DTA (Differential Thermal Analysis) and viscosity measurements. The thin films were structurally characterized by XRD (X-Ray Diffraction), morphologically characterized by SEM (Scanning Electron Microscopy) and TEM (Transmission Electron Microscopy). Moreover, the UV-VIS spectroscopy was used for optical characterization and VSM (Vibrating Sample Magnetometer) for magnetic characterization.

In Table 4.1, some experimental details of the samples that were prepared during this thesis are given. In this study, samples were prepared in order to examine the formation of maghemite thin films and investigate maghemite - hematite transition with changing experimental parameters. Since quartz and glass substrates gave same results, throughout this report only the results for the glass substrates were given.

Table 4.1. Experimental details of the samples which were prepared during the study.

Spin Coating Speed	Drying	Heat Treatment Applied	No. of Layers	Substrate	Sample No
1400 rpm	110 °C 15 min	300 °C for 1 h	1	Glass	41
4000 rpm	110 °C 15 min	300 °C for 1 h	1	Glass	42
1400 rpm	110 °C 15 min	300 °C for 1 h	1	Quartz	40
1400 rpm	110 °C 15 min	300 °C for 1 h	3	Glass	73
1400 rpm	110 °C 15 min	300 °C for 1 h	3	Quartz	72
4000 rpm	110 °C 15 min	300 °C for 1 h	5	Glass	118
4000 rpm	110 °C 15 min	300 °C for 2 h	1	Glass	92
4000 rpm	110 °C 15 min	300 °C for 2 h	3	Quartz	93
1400 rpm	110 °C 15 min	300 °C for 4 h	1	Glass	77
4000 rpm	110 °C 15 min	300 °C for 4 h	1	Glass	78
1400 rpm	110 °C 15 min	300 °C for 4 h	1	Quartz	44
1400 rpm	110 °C 15 min	300 °C for 4 h	3	Glass	76
1400 rpm	110 °C 15 min	300 °C for 4 h	3	Quartz	75
1400 rpm	110 °C 15 min	350 °C for 1 h	1	Glass	102
4000 rpm	110 °C 15 min	350 °C for 1 h	1	Glass	103
1400 rpm	110 °C 15 min	350 °C for 1 h	3	Glass	81
4000 rpm	110 °C 15 min	350 °C for 1 h	3	Glass	104
1400 rpm	110 °C 15 min	350 °C for 1 h	3	Quartz	80
1400 rpm	110 °C 15 min	350 °C for 1 h	4	Glass	114
4000 rpm	110 °C 15 min	350 °C for 1 h	5	Glass	117
1400 rpm	110 °C 15 min	350 °C for 1 h	20	Glass	99
1400 rpm	110 °C 15 min	350 °C for 4 h	1	Glass	89
4000 rpm	110 °C 15 min	350 °C for 4 h	1	Glass	101
1400 rpm	110 °C 15 min	350 °C for 4 h	3	Quartz	88
1400 rpm	110 °C 15 min	350 °C for 4 h	20	Glass	98
1400 rpm	110 °C 15 min	400 °C for 1 h	1	Glass	46
3000 rpm	110 °C 15 min	400 °C for 1 h	1	Glass	48
4000 rpm	110 °C 15 min	400 °C for 1 h	1	Glass	49
1400 rpm	110 °C 15 min	400 °C for 1 h	1	Quartz	47
1400 rpm	110 °C 15 min	400 °C for 1 h	4	Glass	115
4000 rpm	110 °C 15 min	400 °C for 1 h	5	Glass	116
1400 rpm	110 °C 15 min	400 °C for 4 h	1	Glass	69
1400 rpm	110 °C 15 min	400 °C for 4 h	3	Glass	59
1400 rpm	No drying	400 °C for 4 h	3	Glass	60
1400 rpm	110 °C 15 min	400 °C for 4 h	3	Quartz	58
1400 rpm	110 °C 15 min	400 °C for 4 h	8	Quartz	68
1400 rpm	110 °C 15 min	450 °C for 4 h	8	Glass	63
1400 rpm	110 °C 15 min	450 °C for 4 h	8	Quartz	62
1400 rpm	110 °C 15 min	500 °C for 1 h	1	Glass	56
4000rpm	110 °C 15 min	500 °C for 1 h	1	Glass	57
4000rpm	110 °C 15 min	500 °C for 1 h	5	Glass	53
1400rpm	110 °C 15 min	No heat treatment	3	Glass	61
1400rpm	110 °C 15 min	600 °C for 1 h	1	Glass	122
4000rpm	110 °C 15 min	600 °C for 1 h	1	Glass	129

4.1. Solution Properties

As it is stated in the previous chapters, thin film production starts with the preparation of a homogeneous stock solution. This is a very important step for getting crack free films and smooth surfaces. In order to reach these aims, solution preparation step should be carefully carried out.

There are many parameters affecting the quality of the solution such as atmospheric conditions, type of precursor, type of solvent and heating temperature. In this study, experiments were conducted in the laboratory atmosphere. However, glove box conditions may yield better results in order to prevent reactions between air and precursors [43].

Viscosity is an important parameter for the precursor solutions, because it directly affects the homogeneity of the films. Viscosity of the solution S1 with respect to shear rate at 20 °C is given in Figure 4.1. A slight increase in the viscosity was observed at higher shear rates. To determine the behaviour of the solution, power law index was calculated according to equation [2.7]. Power law index value was found as 1.000004333 between 10^2 and 10^3 shear rate values. Since the power law index of the solution is very close to 1, solution S1 was accepted as a Newtonian solution and viscosity of the solution at this temperature was found approximately 0.0035 Pa.s according to Figure 4.1.

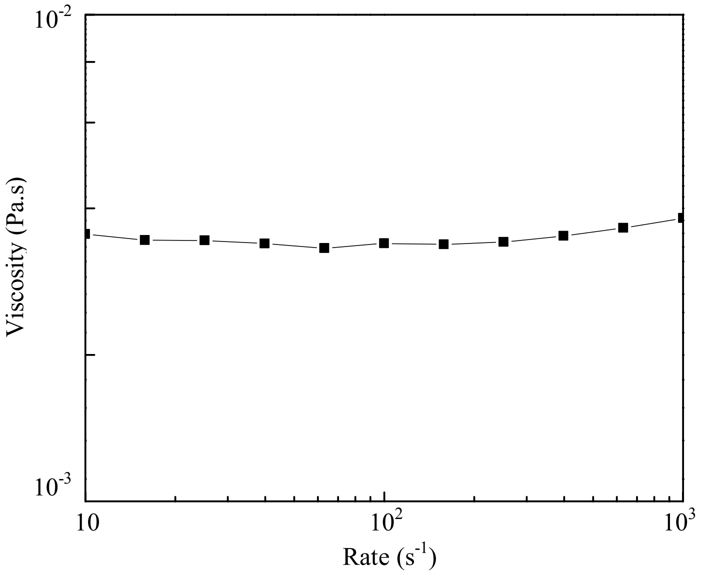

Figure 4.1. Viscosity change of solution S1 at 20 °C with respect to shear rate.

In Figure 4.2, viscosity change with respect to shear rate at 25 °C is given for the same solution S1. In this graph, both a slight decrease and a slight increase were observed. Viscosity decreased at low shear rates, whereas it increased at high shear rates. First and second trends can be assumed as shear-thinning and shear-thickening, respectively. However, the power law indexes for these trends were found as 0.99999625 and 1.0000005. Since they are again very close to 1, the solution S1 at 25 °C also behaved as Newtonian. Viscosity of the solution at this temperature was ~0.0031 Pa.s according to Figure 4.2. All the processes affected by shear rate, such as stirring and spin coating, were performed at room temperature. During these steps, viscosity did not change according to the viscosity measurements. As a result, homogeneous films were obtained by using the solution S1 since homogeneous films were expected from Newtonian fluids [51].

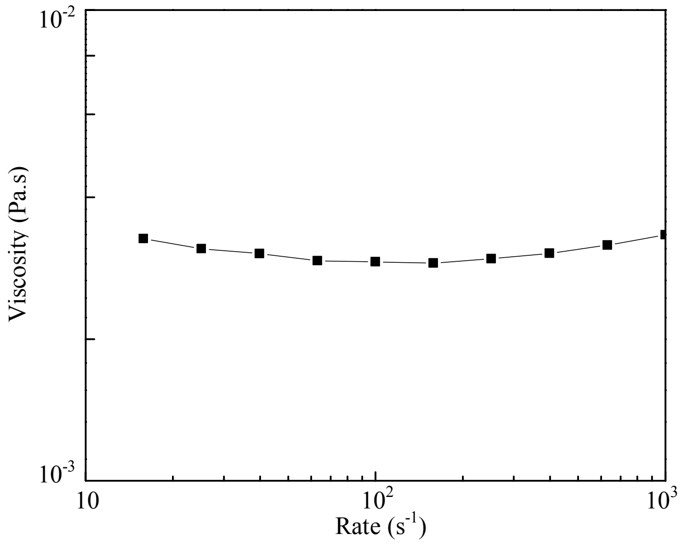

Figure 4.2. Viscosity change of solution S1 at 25 °C with respect to shear rate.

The thermal analysis of the solution also gives significant information about the production procedure of the films. Information on the stability of maghemite can be obtained by DTA and TG analyses. To investigate the thermal stability of maghemite and follow the kinetics of the γ (maghemite) → α (hematite) transition, TG/DTA characterization methods were used.

Figure 4.3 and 4.4 show the TG and DTA curves of the maghemite gel, respectively, which were obtained from room temperature up to 1100 °C by using a heating rate of 3 °C /min. In order to get maghemite powder used in the analysis, solution was dried at 100 °C for 8 hours. The TG curve exhibited three distinct weight loss steps and the DTA curve showed two exothermic peaks. The first weight loss step (approximately 5 %) was in the temperature range of 35 °C and 130 °C, which corresponds to the removal of moisture present in the gel. The second weight loss step (63 % weight loss) was in the temperature range of 130-330 °C. It was assigned to the simultaneous decomposition and oxidation of the FeOOH, intermediate complex of

Fe-O system, and liberation of maghemite [55]. The exothermic peak at approximately 270 °C supported this behaviour. The last weight loss region (2 % weight loss) was between 330 °C and 440 °C and it was due to the phase transition of maghemite to hematite. The exothermic peak at 433 °C in the DTA curve could be attributed to this behaviour. The exothermic peak, without a significant weight loss, is caused mainly by the structural phase transition from the metastable γ phase to the stable α phase.

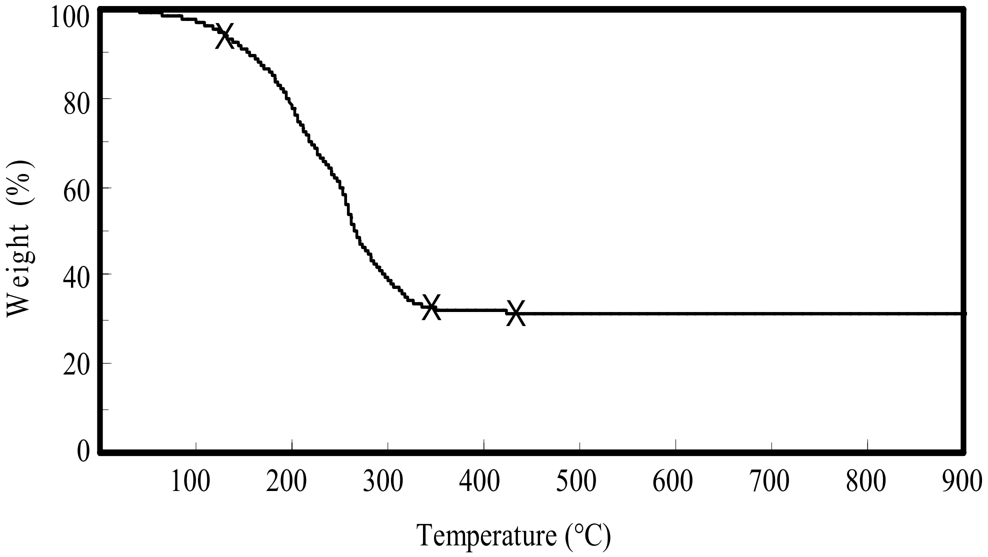

Figure 4.3. TGA curve of the powder sample from solution S1 which was obtained after drying at 100° C for 8 h in air.

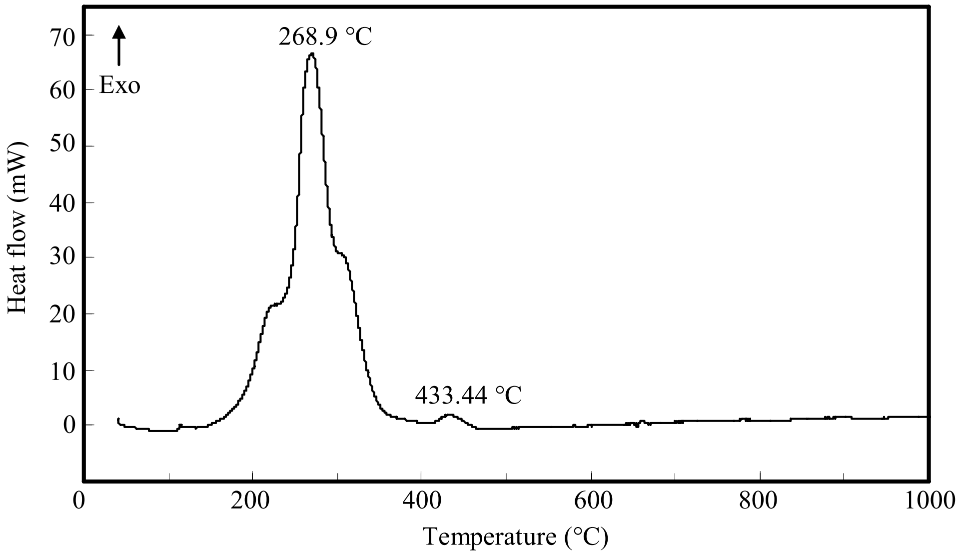

Figure 4.4. DTA result of the powder sample from solution S1 which was obtained after drying at 100 °C for 8 h in air.

In order to investigate the maghemite formation characteristics of the solutions S1, S2 and S3, powders which were obtained from these solutions were examined via XRD. Powders were prepared by drying at 100 °C for 8 hours and annealing at 350 °C for 1 hour. In figure 4.5, powders which were prepared using solution S1 and S2 contained only maghemite phase although powder prepared from S3 began to transform to hematite phase when it was annealed at 350 °C.

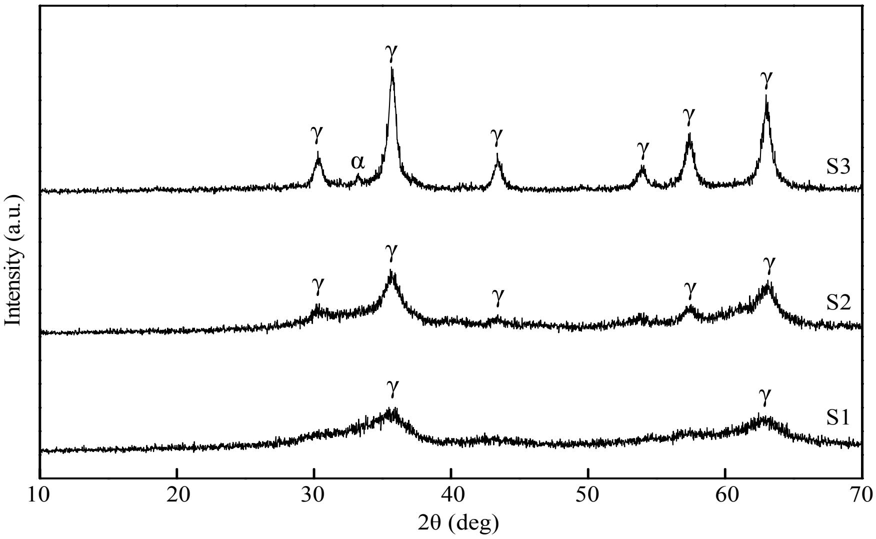

Figure 4.5. XRD spectra of powders (annealed at 350 °C for 1 hour) obtained from the solutions S1, S2 and S3.

Average particle sizes of the powder samples obtained from different solutions were estimated by using Scherrer's Formula, which is a technique based on measuring the full width of x-ray diffraction peaks at the half maximum height of the peak.

$$t = \frac{0.94 \times \lambda}{B \times \cos\theta} \qquad \text{Eq. [4.1]}$$

In the formula, t is the average particle size, λ is the wavelength of radiation of the x-ray beam used, B is the width of the peak at half of the maximum intensity (in radians) and θ is the half of the diffraction angle 2θ [56]. In the calculations, maghemite (311) peak was used as being the most intense peak. Estimated particle sizes of the maghemite powders are given in Table 4.2. It can be observed from this table that, the first solution S1 yielded the smallest particle size without giving any hematite peak, thus solution S1 was selected as the main solution used for the experiments throughout the study.

Table 4.2. Approximate particle sizes of iron oxide powders obtained from the solutions.

$t = \dfrac{0.94 \times \lambda}{B \times \cos\theta}$	**Powder from Solution S1**	**Powder from Solution S2**	**Powder from Solution S3**
Approximate Particle Size	2.1 nm	4.2 nm	7.2 nm

4.2. Thin Film Preparation

Thin film preparation starts with substrate preparation. Without obtaining effective coherent adhesion between the substrate and the film, thin films are useless. But the only important parameter is not the adhesion. Choosing a proper substrate is also another important factor to get proper films. Alumina and pure silica were also used as substrates for maghemite thin films but the adhesion of films onto these substrates was not effective. The glass and quartz substrates which were prepared by piranha solution gave better results than the substrates which were prepared by ultrasonic cleaning. In Figure 4.6, SEM micrograph of a glass substrate which was prepared by ultrasonic cleaning can be seen. The surface of the substrate is smooth and no major impurities were observed. On the other hand, some impurities on the surface of the glass substrate, which was prepared by piranha solution, were detected in Figure 4.7. During the etching process surface area of the sample increases and this causes higher surface energy. As a result, much attention should be given to etched substrates during coating since the surface of the substrate is more attractive and more sensitive to environmental effects.

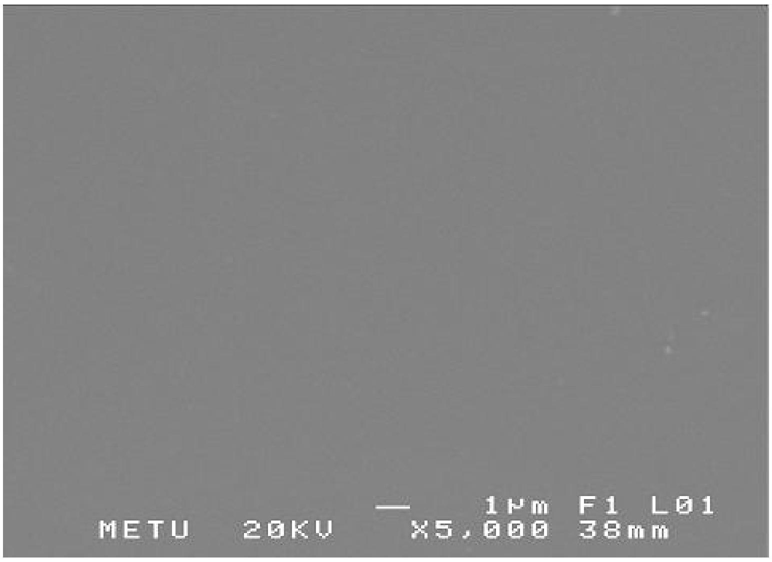

Figure 4.6. SEM micrograph of glass substrate which was not etched.

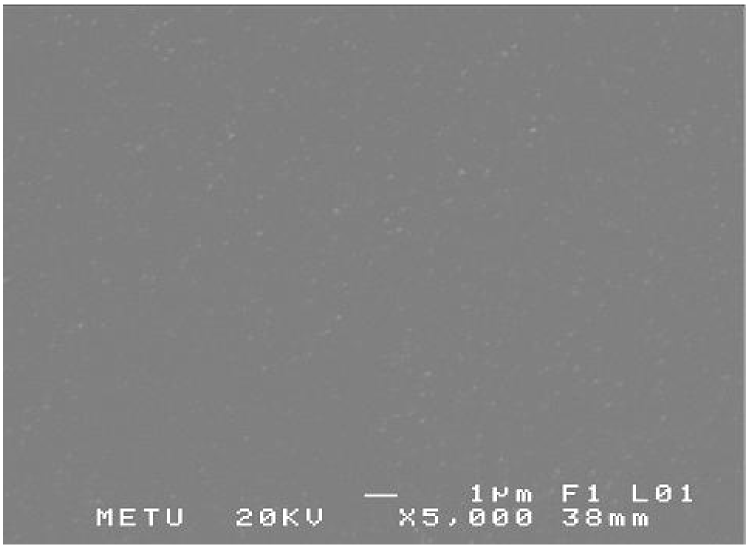

Figure 4.7. SEM micrograph of etched glass substrate.

Although the surface morphologies were different, there was no difference in their chemical composition, which indicated that no unwanted chemicals were left after the etching process. The EDS analysis of the etched glass sample was given in Figure 4.8.

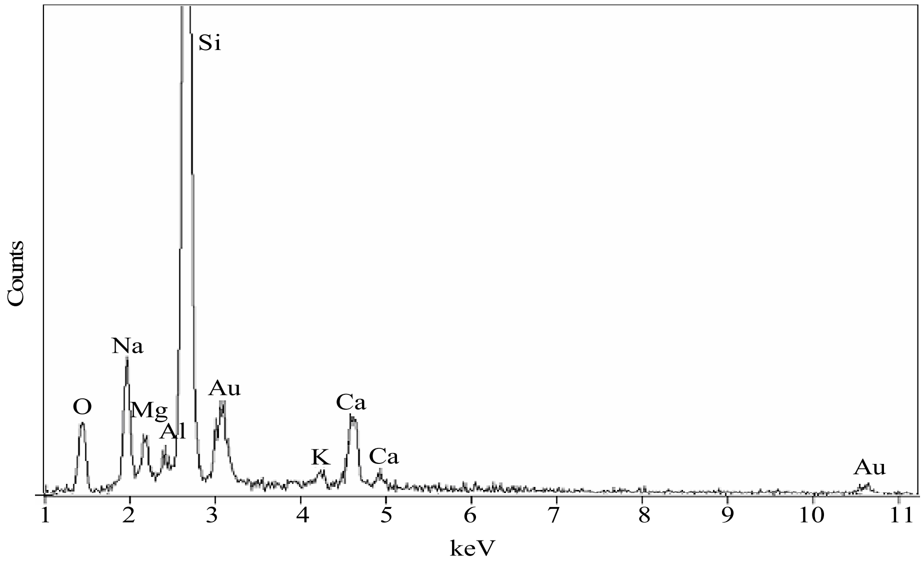

Figure 4.8. EDS analysis of the etched glass substrate.

4.3. Morphology of the Films

The surface morphology of the films on glass substrates, annealed at different temperatures is studied by using SEM. Most of the films had homogeneous and crack free surfaces similar to the sample which was given in Figure 4.9. The SEM micrograph belongs to single-layered sample which was annealed at 350 °C for 1 hour. Higher annealing temperatures or multi-layer coatings may yield crack formation. Crack formation of a three-layered sample, which was annealed at 350 °C for 1 hour can be seen in Figure 4.10. Although this sample was annealed at the same heat treatment conditions with the sample given in Figure 4.9, multicoating steps caused local cracks. The heat treatment applied after each layer can be the reason for these cracks. Another possible cause for the development of cracks can be the thermal mismatch between the substrate and the film [38].

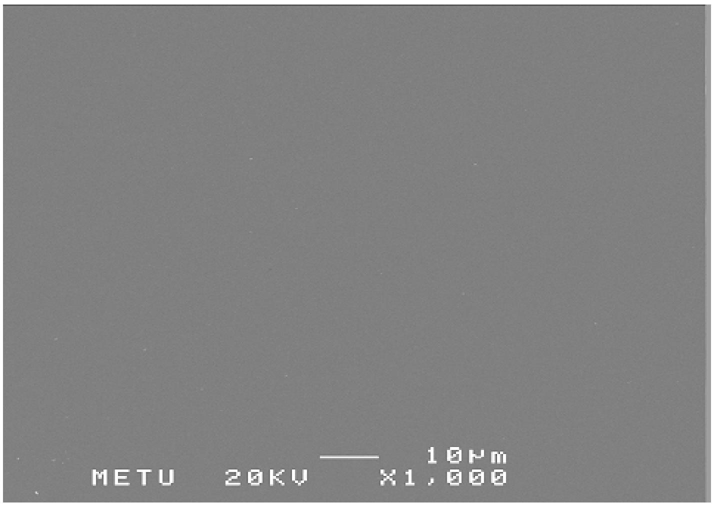

Figure 4.9. SEM micrograph of a single layered film surface which was coated on a glass substrate.

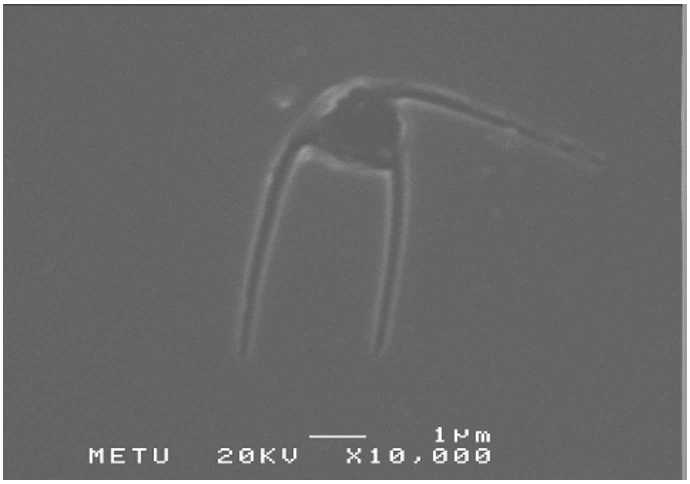

Figure 4.10. SEM micrograph of a multi-layered film surface which was coated on a glass substrate.

The estimated one layer thickness of a three layered iron oxide thin film which was prepared at a spinning rate of 4000 rpm was 65 nm and the total thickness of three layered sample was also found approximately 190 nm. The cross sectional view of this sample is given in Figure 4.11. SEM micrograph of the cross sectional view of the single layered sample, which was prepared at a spinning rate of 1400 rpm has approximately 80 nm thickness as given in Figure 4.12. Thickness of this film was also determined through its cross sectional view by using a Field Emission SEM (Zeiss Supra). Similar thickness value was found as seen in Figure 4.13. Both one layered and three layered samples were annealed at 350 °C for 1 hour. Lower spinning rates yield higher thickness values.

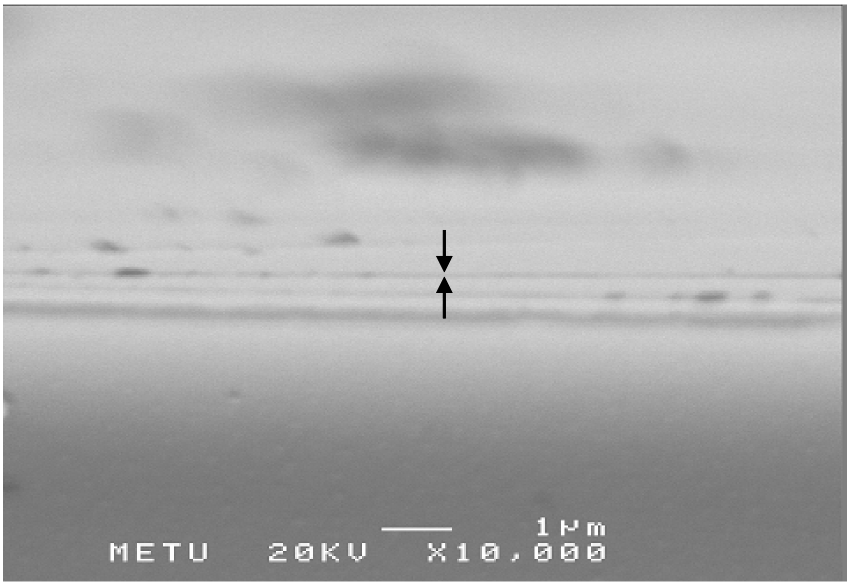

Figure 4.11. Cross sectional SEM micrograph of the three-layered film (total thickness ~190 nm) coated at 4000 rpm.

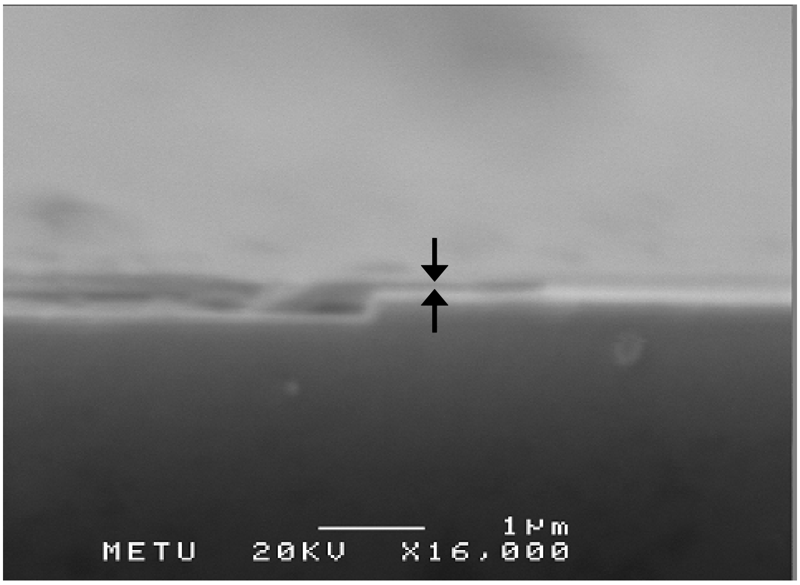

Figure 4.12. Cross sectional SEM micrograph of the single-layered film (~80 nm) on a glass substrate coated at 1400 rpm.

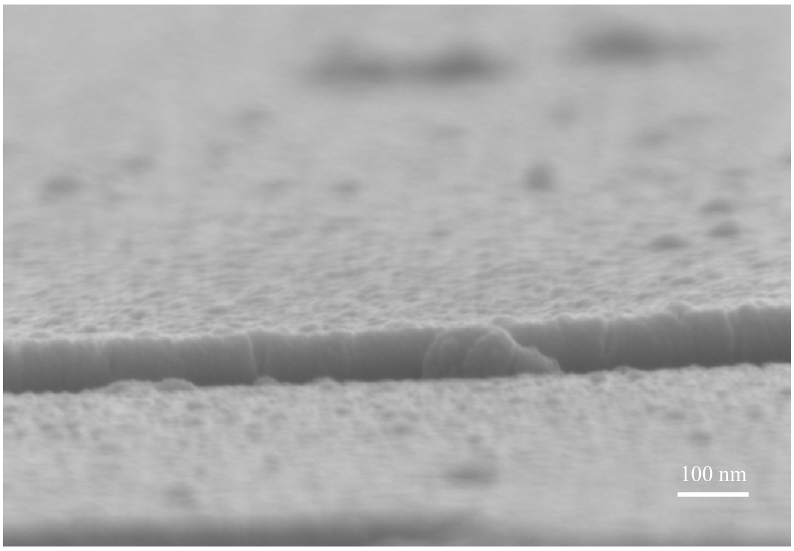

Figure 4.13. Cross sectional FE-SEM micrograph of the single-layered film (~80 nm) on a glass substrate coated at 1400 rpm (Magnification was x 5.10^4).

EDS analyses, which were taken from different areas of the film gave similar elemental compositions, which verified the chemical homogeneity of the produced films. The EDS analysis given in Figure 4.14 belongs to three layered (~190 nm) sample which was annealed at 400 °C for 1 hour. The EDS analysis of the one layered sample (~65 nm) which was heat treated and coated using the same parameters, is given in Figure 4.15. The EDS analysis of the three layered (~190 nm) sample showed a higher Fe peak than EDS analysis of one layered (~65 nm) sample. This can be explained by the substrate effect. The chemical species present in the substrate are more dominant in the EDS spectra for thinner films compared to thicker ones.

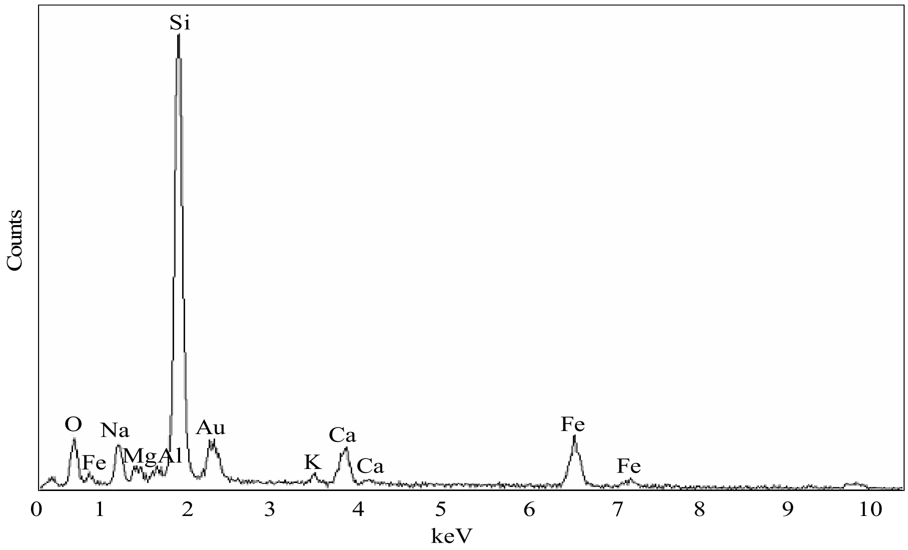

Figure 4.14. EDS analysis of three-layered film (~190 nm) which was annealed at 400 °C for 1 hour.

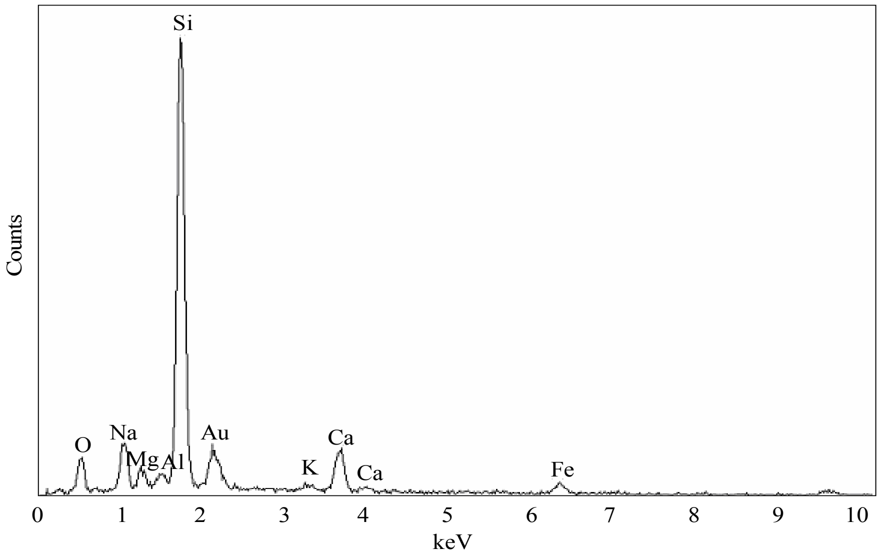

Figure 4.15. EDS analysis of single-layered film (~65 nm) annealed at 400 °C for 1 hour.

4.4. Structure of Maghemite Thin Films

Heat treatment of the film is a key parameter to produce crack free, homogeneous and crystalline thin films. The drying step was used to remove water without causing any crack formation. Moreover, annealing was performed to produce the required crystalline phase.

4.4.1. Effect of the Annealing Temperature on the Maghemite Formation

Different types of annealing conditions were applied to the films in order to investigate the maghemite formation. To examine the temperature effects, thin films were sintered at 300°C, 350°C, 400°C and 500°C for 1 hour.

4.4.1.1. XRD Study

In Figure 4.16, XRD patterns of iron oxide thin films with respect to increasing annealing temperature are given. All films were coated at 1400 rpm and their thicknesses are approximately 80 nm according to SEM results.

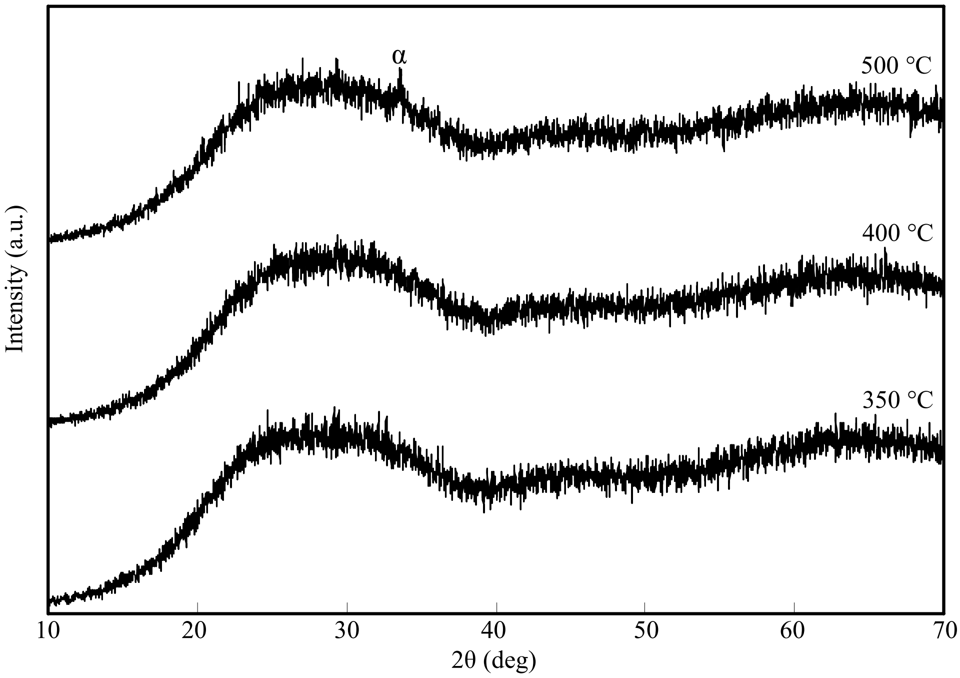

Figure 4.16. XRD spectra of single layered thin films (~80 nm) annealed at different temperatures for 1 hour.

As it was observed from Figure 4.16, maghemite phase was not detected by XRD although hematite phase was detected because of two reasons. First reason is the nanoscale maghemite phase. It is known from the literature that maghemite phase transforms to hematite with increasing grain size [49]. With increasing annealing temperature, grain size increases and this lets the maghemite phase in the thin films to transform to hematite. The peak observed in the Figure 4.16 belongs to hematite (104) plane. To understand the typical grain size of hematite phase, grain size of the sample annealed at 500 °C was estimated by Scherrer's Formula. From the equation [4.1], the grain size was found as approximately 2.9 nm. The expected maghemite phase grain size is lower than this value. Geometrically, the grain sizes less than 2 nm can not easily be detected by x-ray diffraction method. Thus, nanoscale maghemite phase may not be detected using conventional powder x-ray diffraction method although relatively larger scale hematite phase can be detected. In addition, amorphous behaviour of iron oxide thin films at lower temperatures is explained by the formation of nanoscale maghemite phase in the films in several references [34, 35, 37, 40]. The presence of maghemite in these films was shown by using TEM as explained in the next section. Second reason is the film thickness. Substrate dominates the XRD patterns since the produced thin films thicknesses were between 65 nm and 80 nm. The effect of the substrates can be eliminated by parallel beam method XRD which will be given in section 4.5.

4.4.1.2. TEM study

TEM micrograph which was given in Figure 4.17.a shows the morphology of the single-layered thin film (~80 nm). The film was annealed at 350 °C for 1 hour. The TEM sample was prepared by scraping the film off the surface. Since the film onto the etched substrate is more adhesive, the TEM samples were prepared from films coated on substrates that are not etched. The electron diffraction pattern of this sample is given in Figure 4.17.b.

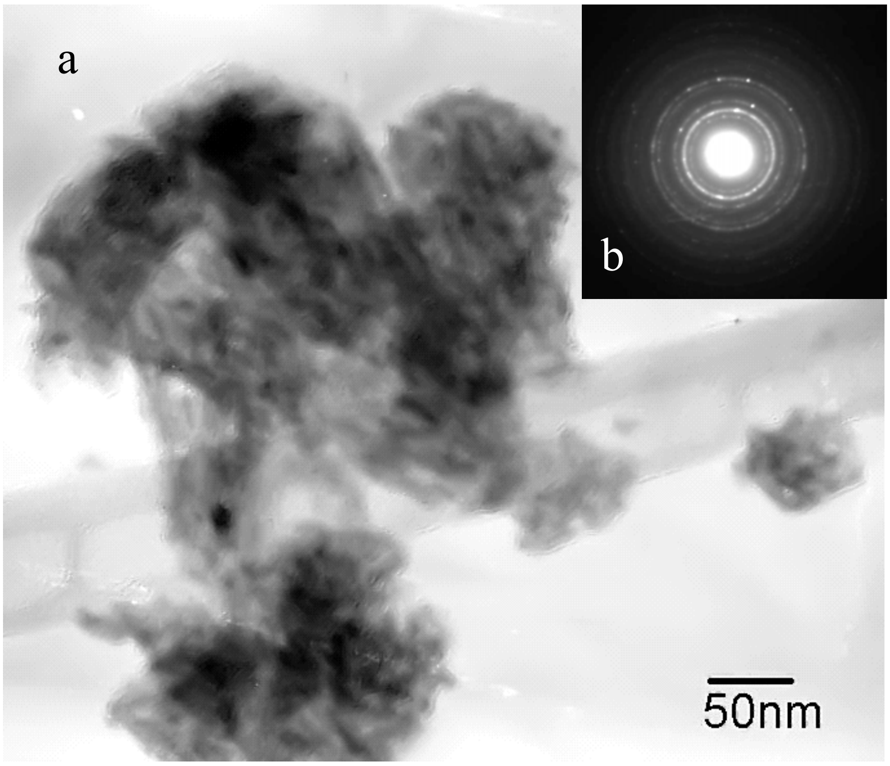

Figure 4.17. (a) TEM micrograph and **(b)** electron diffraction pattern of the single-layered maghemite thin film (~80 nm) which was annealed at 350 °C for 1 hour.

The TEM constants for the sample characterization was λ= 0.019 A^o for 300 kV and L = 100 cm where L is camera length. The interplanar spacings of the sample were calculated by using the radii in the diffraction pattern from equation [4.4]. This equation is found from the Bragg law and simple geometrical equation which are given in equations [4.2] and [4.3]. For the small angles Bragg law is [57];

$$\lambda = 2d\theta \qquad \text{Eq. [4.2]}$$

Geometrically;

$$\frac{R}{L} = 2\theta \qquad \text{Eq. [4.3]}$$

By combining equation [4.2] and [4.3]

$$\frac{R}{L} = \frac{\lambda}{d} \qquad \text{Eq. [4.4]}$$

Table 4.3. The measured radii and calculated d_{hkl} of the sample (~80 nm) annealed at 350 °C for 1 hour.

Measured Radius	**d_{hkl}**
$R_1 =$ 6.4 mm	$d_1 = 2.96$ A^o
$R_2 =$ 7.6mm	$d_2 = 2.5$ A^o
$R_3 =$ 9.1mm	$d_3 = 2.087$ A^o
$R_4 =$ 11.9mm	$d_4 = 1.596$ A^o
$R_5 =$ 12.9mm	$d_5 = 1.473$A^o

The resultant interplanar spacings of the sample are given in Table 4.3. The crystal structure of the maghemite phase is cubic. For cubic structures the interplanar spacing can be calculated theoretically from equation [4.5]. In Table 4.4, the comparison of the observed and theoretical interplanar spacings is given.

$$d_{hkl} = \frac{a_o}{\sqrt{h^2 + k^2 + l^2}} \qquad \text{Eq. [4.5]}$$

Table 4.4. The observed and theoretical interplanar spacings of the sample (~80 nm) which was annealed at 350 °C for 1 hour.

d_{hkl} (observed)	hkl (maghemite)	d_{hkl} (evaluated)
2.96	220	2.953
2.5	311	2.518
2.087	400	2.088
1.596	511	1.607
1.473	440	1.476

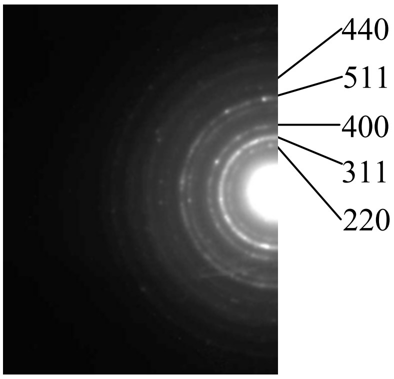

Figure 4.18. Electron diffraction pattern and its interpretation for single layered (~80 nm) maghemite thin film annealed at 350 °C for 1 hour.

It was seen from Table 4.4 and Figure 4.18 that the observed ring pattern belongs to maghemite phase. Other TEM samples which were prepared from the same thin film gave the same result. Another TEM micrograph of the same maghemite film is given in Figure 4.19. Corresponding electron diffraction pattern is shown in the inset. Thus, the single layered samples (~80 nm) which were annealed at 350 °C for 1 hour were determined to be maghemite thin films.

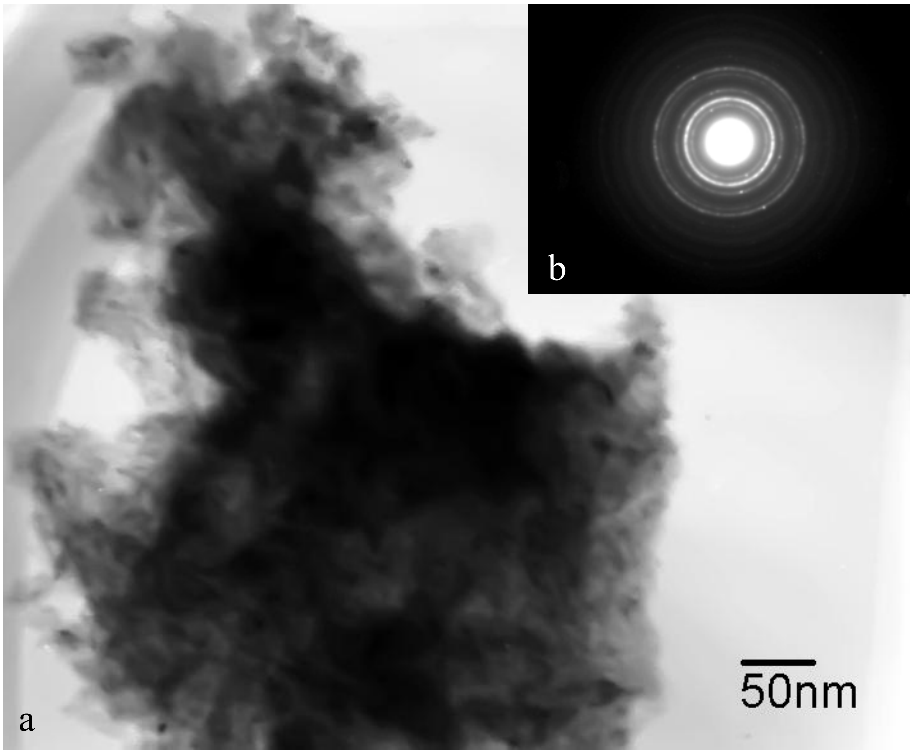

Figure 4.19. (a) TEM micrograph and **(b)** electron diffraction pattern of single layered (~80 nm) maghemite thin film annealed at 350 °C for 1 hour.

TEM micrograph of a single layered sample (~80 nm) annealed at 500 °C for 1 hour is given in Figure 4.20. From Figure 4.16, this sample was detected as hematite thin film. However, according to selected area electron diffraction (SAED) pattern which is given in Figure 4.20.b, this film also contained maghemite phase. The point patterns belonged to maghemite phase with [001] zone axis. To find the indices of the point pattern given in Figure 4.20.b, the same relations were used with ring pattern. From the equation [4.4], the interplanar spacings were calculated for R_1, R_2 and R_3. Since R_1 and R_2 are the same, the resultant interplanar spacing is found as 3.393 Å. The measured radii and calculated interplanar spacings are given in Table 4.5.

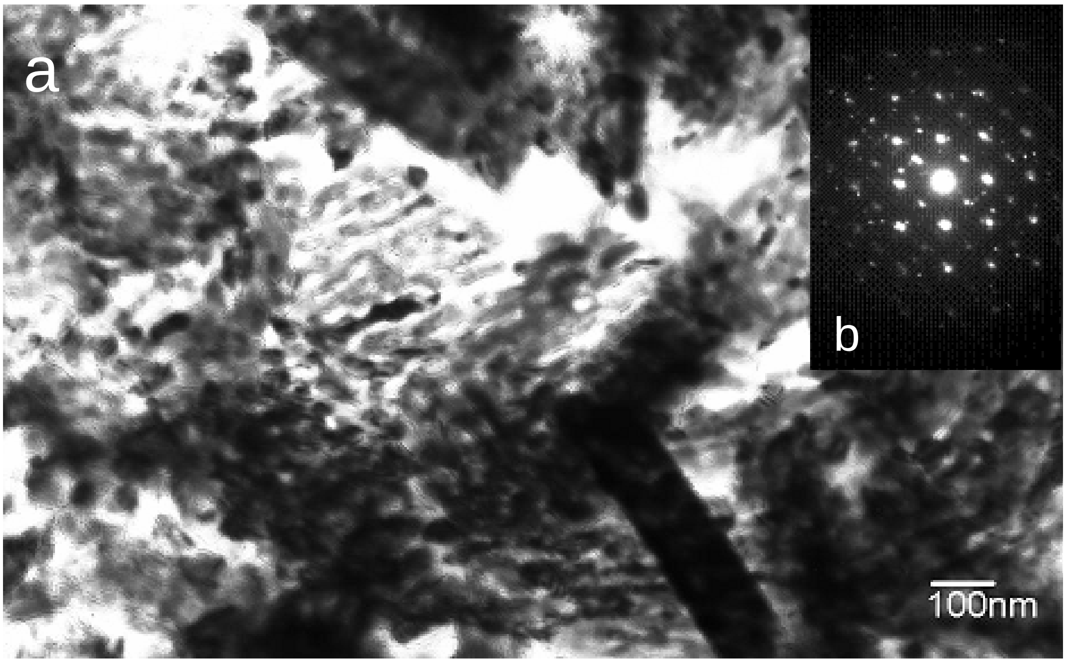

Figure 4.20. (a) TEM micrograph and **(b)** selected area electron diffraction (SAED) pattern of the single layered film (~80 nm) annealed at 500 °C for 1 hour.

Table 4.5. The measured radii and calculated d_{hkl} of the sample (~80 nm) annealed at 500 °C for 1 hour.

Measured Radius	$\mathbf{d_{hkl}}$
R_1=5.6 mm	d_1=3.393 A^o
R_2=5.6 mm	d_2=3.393 A^o
R_3=6.5 mm	d_3=2.923 A^o

From reciprocal plane modelling of maghemite, this interplanar spacing belongs to <112> family of planes. According to equation [4.5], the lattice parameter is calculated as 8.311 Å. This value is very close to theoretical maghemite lattice parameter, which is between 8.3 and 8.38 [58]. The third measured interplanar spacing has to be checked by reverse calculation in order to state that the SAED belongs to maghemite phase. From the reciprocal plane modelling, the third calculated interplanar spacing belongs to <202 > family of planes. From the equation [4.5], the interplanar spacing was found as 2.938. This value satisfied the interplanar spacing which was calculated from the measured radius. In Figure 4.21, electron diffraction pattern and the reciprocal plane modelling of the film is given.

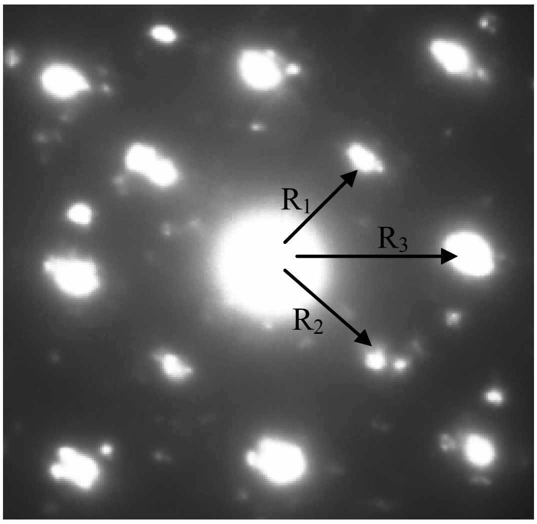

Figure 4.21. Selected area electron diffraction pattern (SAED) of the film annealed at 500 °C for 1 hour.

Another TEM micrograph and selected area electron diffraction pattern of the same sample are given in Figure 4.22. The SAED shows that film consisted of mixture of maghemite and hematite phases. As a result, although the film annealed at 500 °C for 1 hour had only hematite phase in XRD results, it was observed that the film had a mixture of hematite and maghemite phases in TEM results.

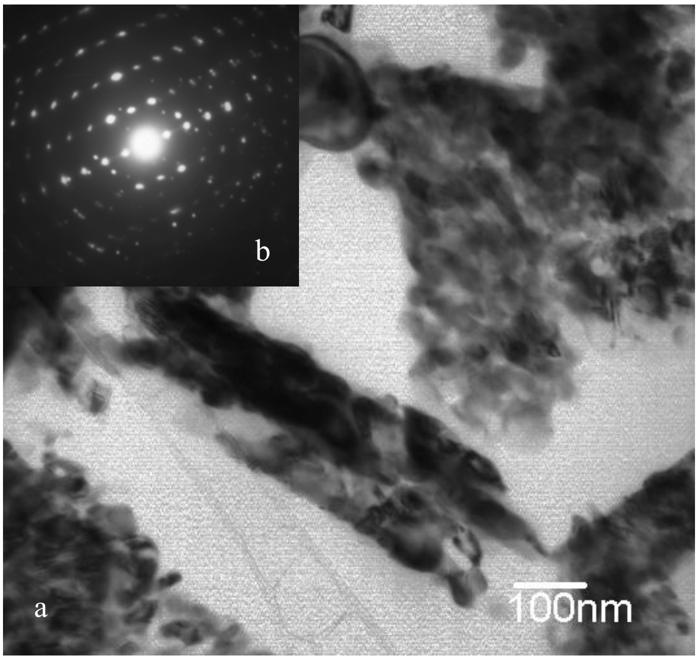

Figure 4.22. (a) TEM micrograph and **(b)** selected area electron diffraction (SAED) pattern of the film which was annealed at 500 °C for 1 hour.

In conclusion, nanoscale maghemite phase can not be observed by XRD method although its presence was proved by TEM. Since the maghemite phase transforms to hematite phase with increasing grain size, hematite can be detected by XRD unlike nanoscale maghemite phase. From the TEM results, the sample annealed at 350 °C for 1 hour was maghemite thin film. Whereas, the film annealed at 500 °C for 1 hour was containing both hematite and maghemite phases according to TEM analysis although it was observed as hematite by XRD (Figure 4.16).

4.4.2. Effect of the Annealing Time on the Maghemite Formation

Annealing time is another parameter for maghemite thin film production. It has the same effect with annealing temperature since the grain size increases when annealing time increases.

4.4.2.1. XRD study

Samples which were annealed at 350 °C and 400 °C for 4 hours were given in Figure 4.23. In the figure, single layered (~80 nm) thin film, annealed at 400 °C, showed hematite phase formation. However, in Figure 4.16, hematite transition was observed only in sample annealed at 500 °C for 1 hour. It is known that γ-Fe_2O_3 is metastable and easily transforms into α-Fe_2O_3 on annealing for long periods [59]. Thus, maghemite phase is more stable when it is annealed for short annealing periods, whereas hematite phase started to appear with the increase in annealing time. The change in the XRD spectra of the sample which was annealed at 400 °C for 1 and 4 hours can be seen in Figure 4.24.

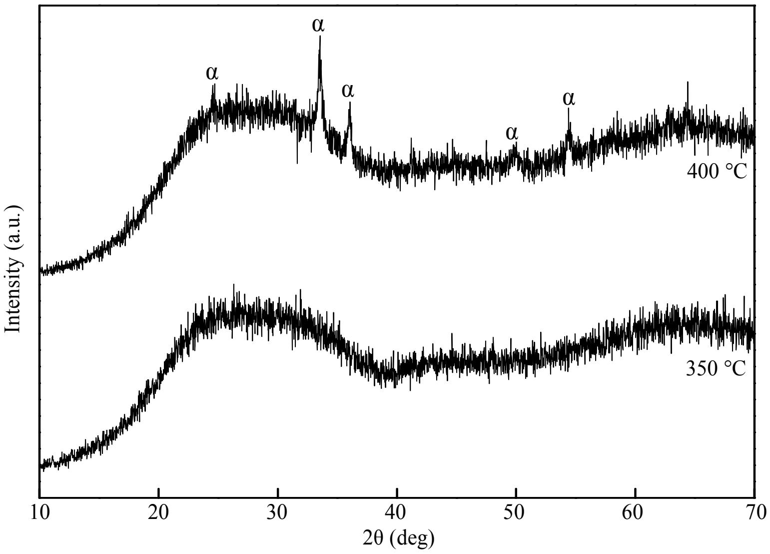

Figure 4.23. XRD spectra of single layered (~80 nm) thin films annealed at different temperatures for 4 hour.

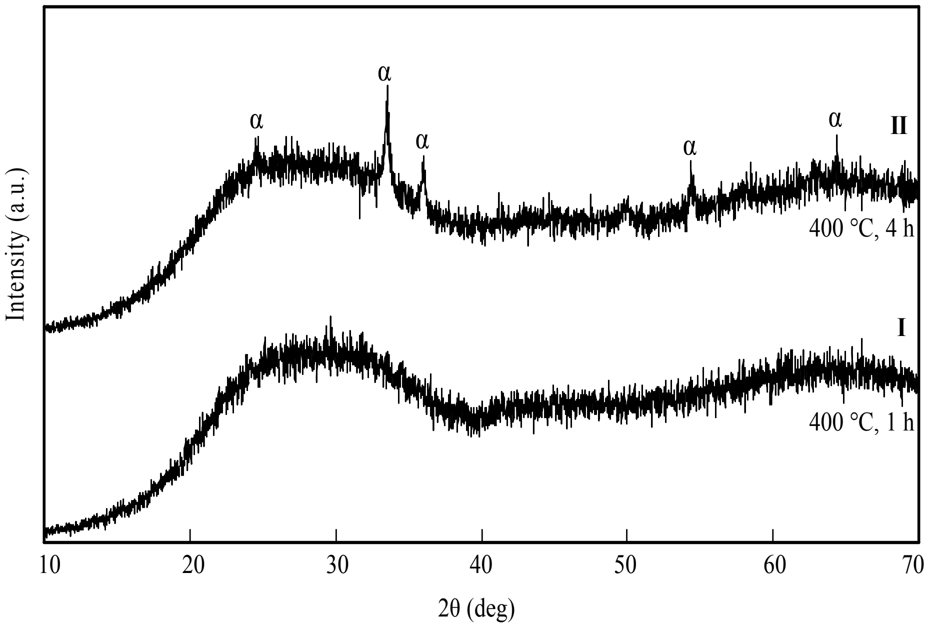

Figure 4.24. XRD spectra of single-layered (~80 nm) thin films annealed at 400 °C for different periods.

At relatively low temperatures, maghemite to hematite transition with increasing annealing time was not observed. In Figure 4.25 two samples which were annealed at 350 °C for different time periods are given. According to Figure 4.25, hematite phase was not observed even after annealing for 4 hours. So, the annealing time is an important factor for hematite formation but the controlling factor is the annealing temperature.

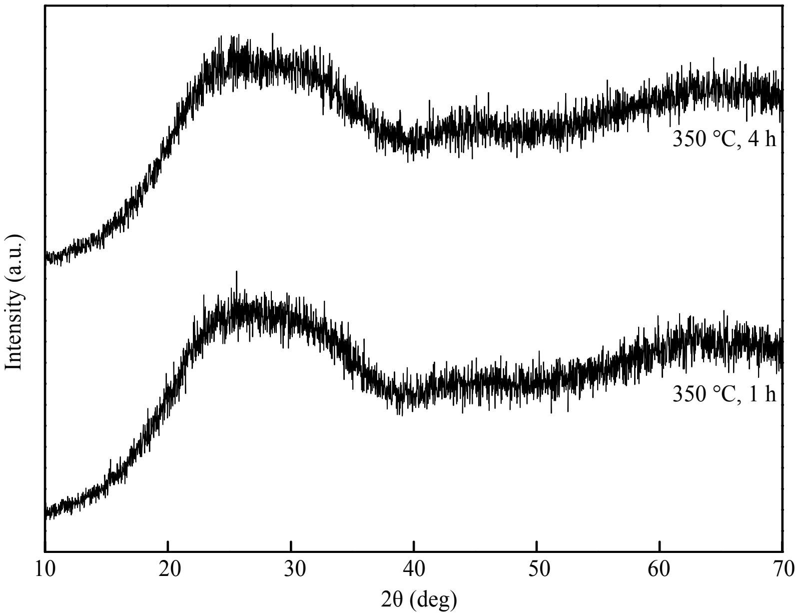

Figure 4.25. XRD spectra of single-layered (~80 nm) thin films annealed at 350 °C for different periods.

4.4.3. Effect of Film Thickness on the Maghemite Formation

The effect of the film thickness is different from other experimental parameters because the basic aim of this study is to prepare thin films having thicknesses in nanometer range. One layer thickness of a sample which was prepared at a spinning rate of 1400 rpm was ~80 nm and a sample which was prepared at a spinning rate of 4000 rpm was ~65 nm. These values are typical for a thin film and production of the thicker films was not desired in the study. However, effect of the thickness on maghemite formation can not be neglected so it was also examined in relation to other parameters.

In Figure 4.26, two samples, A and B, showed different x-ray spectra because of the difference in the film thickness although the heat treatment conditions of the samples were the same. Sample A was a one-layered sample (~65 nm), whereas sample B was 5-layered sample (~300 nm) and they were both annealed at 400 °C for 1 hour. Due to the fact that multi-layered films are subjected to a total thermal treatment time longer than that of the single layered films, hematite phase was only detected in sample B (~300 nm) in Figure 4.26. In multi-layered films, following layers crystallize more readily as being deposited on a previously annealed film layer [60]. Moreover, as the film thickness increases, bulk diffusion tends to increase and small grains tend to coalesce to form larger grains. Consequently, maghemite more easily transformed to hematite in multi-layered films and higher thicknesses are not desired for maghemite thin films.

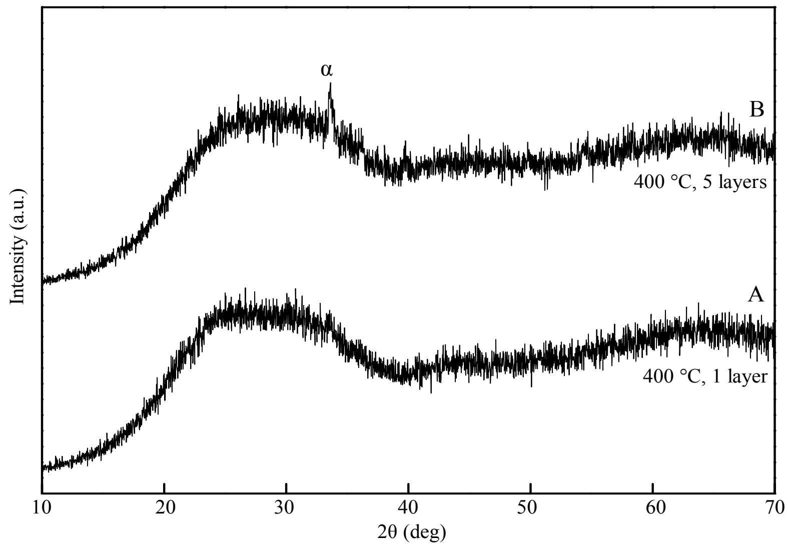

Figure 4.26. XRD spectra of single (~65 nm) and 5-layered (~300 nm) thin films annealed at 400 °C for 1 hour.

Like the effect of the annealing time, the effect of the film thickness is not as effective as the effect of the annealing temperature on the maghemite formation. At low temperatures the hematite phase formation was not observed with increasing film thickness. In Figure 4.27, the hematite transition was not detected even the film annealed at 350 °C for 1 hour was twenty layers (~1.5 μm).

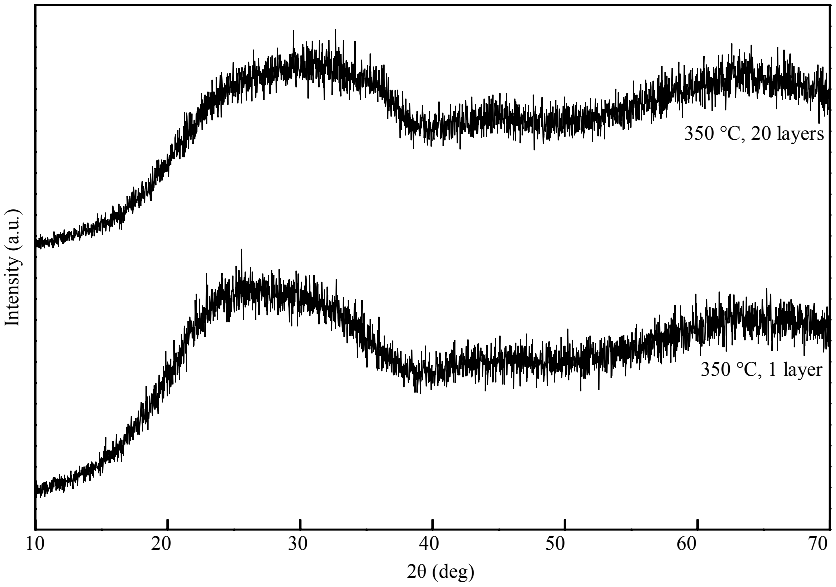

Figure 4.27. XRD spectra of single (~80 nm) and 20-layered (~1.5 μm) thin films annealed at 350 °C for 1 hour.

When annealing time and thickness were both increased, they become more effective in hematite formation. In Figure 4.28, the maghemite phase transformed to hematite after annealing 4 hours at 350 °C for twenty layered sample (~1.5 μm). So, according to Figure 4.25 and 4.27 that lower annealing time and/or lower sample thickness favored the maghemite formation.

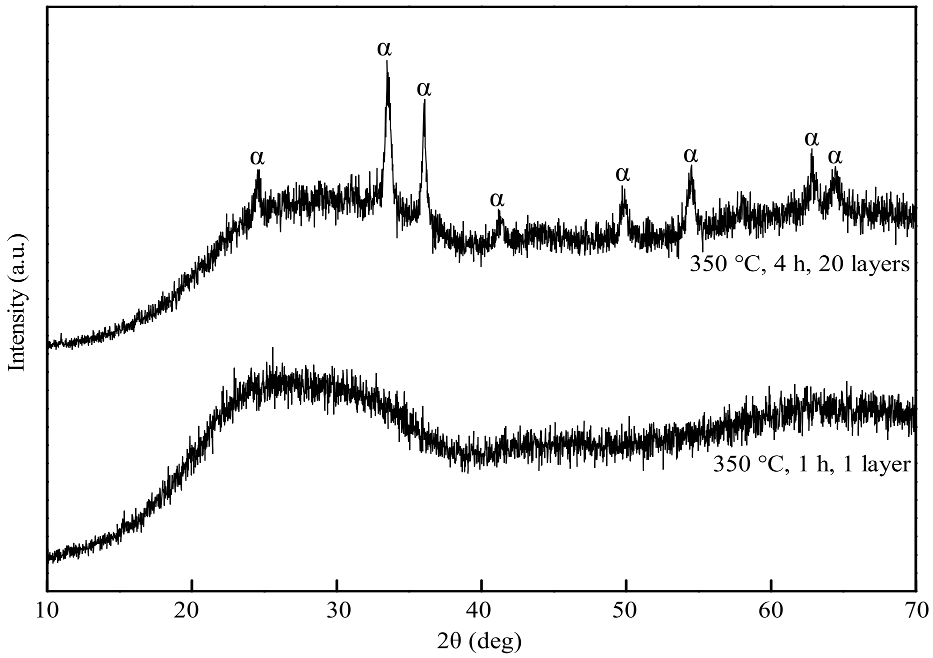

Figure 4.28. XRD spectra of single (~80 nm) and twenty-layered (~1.5 μm) films annealed at 350 °C for 1 hour and 4 hours, respectively.

4.5. Parallel Beam Method

Parallel beam method was applied to some samples to investigate the structural properties of the thin film and decrease the effect of the substrates. Since substrates affect x-ray diffraction results of the thin films, the parallel beam method was utilized by using different incidence angles and divergence slits. The height limiting divergence slit was chosen as 5 mm during all experiments.

In Figure 4.29, the maghemite thin film (~80 nm) annealed at 350 °C for 1 hour, was examined with parallel beam method as well as focusing method. The incidence angle and the divergence slit were chosen as 0.3 ° and 0.1, respectively according to equation [3.5] in the first case. In the second case, incidence angle was selected as 1°

without changing divergence slit. The focusing method result of the sample is also given. The basic aim of the parallel beam method is to dispose of the substrate effect and this aim is achieved but intensity is also reduced as it was observed in Figure 4.29.

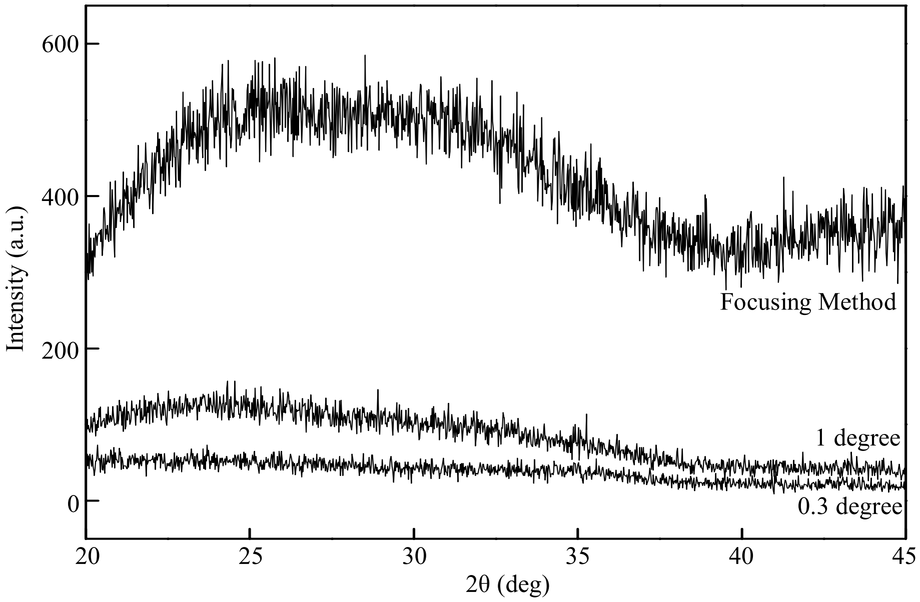

Figure 4.29. XRD spectra of maghemite thin film (~80 nm) annealed at 350 °C for 1 hour. Both Parallel Beam and Focusing Methods were applied.

Intensity reduction of the sample, annealed at 400 °C for 1 hour, can be observed more clearly in Figure 4.30. The incidence angle and the divergence slit were chosen as 1 ° and 0.1, respectively. Because the intensities of the nanostructured samples are low, parallel beam method is not practical for nanostructured maghemite thin films.

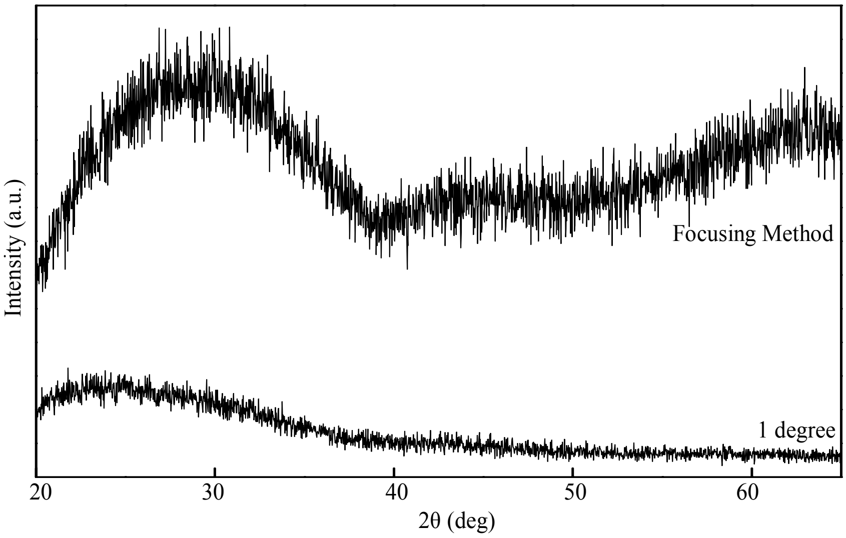

Figure 4.30. XRD spectra of thin film (~80 nm) annealed at 400 °C for 1 hour. Both Parallel Beam and Focusing Methods were applied.

4.6. Optical Properties of Maghemite Thin Films

Since maghemite thin films are highly transparent, they are finding increasing commercial use for optical data storage devices in compact discs and computer memory applications. Thus, the optical characterization of maghemite thin films is crucial. Moreover, with phase transition, the optical properties deteriorate, maghemite to hematite transition affects the optical properties and this effect also needs to be investigated.

The spectral transmittance of one layered sample (~80 nm) which were dried at 110 °C, annealed at 300 °C, 400 °C and 500 °C for 1 hour is given in Figure 4.31 and the spectrum of the same specimen annealed at 350 °C is given in Figure 4.32 as a function of the wavelength. The sample which was dried only, gave 90 % transmittance in the wavelength range 450-800 nm. The samples annealed at 300 °C and 350 °C for 1 hour gave more than 90 % transmittance values for above 600 nm, whereas for samples which were annealed at 400 °C and 500 °C for 1 hour, transmittance values were less than the other samples. As the annealing temperature increases, a steeper optical edge is better defined. It is detected from Figure 4.31 that highly transparent iron oxide thin films were produced by annealing at lower temperatures. Increasing the annealing temperature provided the formation of hematite phase in the films as indicated by XRD spectra and caused the decrease in the transmittance values.

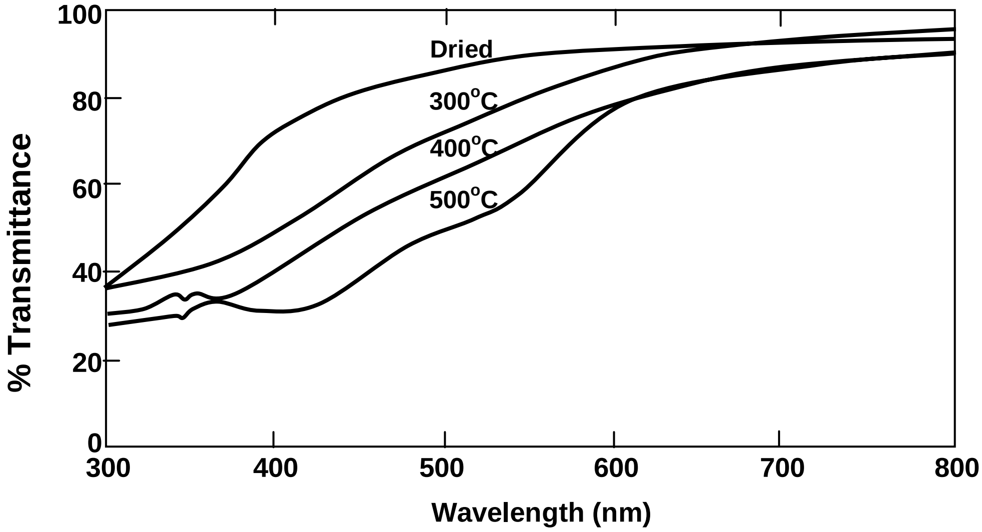

Figure 4.31. UV-visible spectra of thin films (~80 nm) annealed at different temperatures.

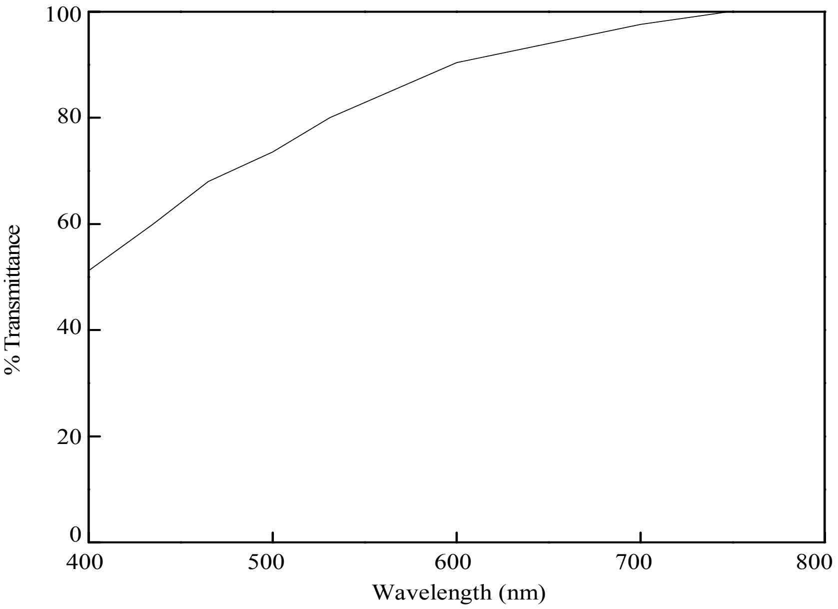

Figure 4.32. UV-visible spectra of the maghemite thin film (~80 nm) annealed at 350 °C for 1 hour.

The thin films (~80 nm) which were annealed at 350 °C and 400 °C for 1 hour were examined to find absorbance coefficient, extinction coefficient and optical band gap.

The transmittance of the films exhibited characteristic of inter-band transitions. The band-to-band transitions are described by the relation [53];

$$\alpha(h\nu) = A(h\nu - E_g)^n \qquad \text{Eq. [4.6]}$$

where $\alpha(h\nu)$ is the absorption coefficient, A is a constant, which does not depend on photon energy, n depends on the nature of optical transition, $h\nu$ the photon energy and E_g is the band gap. The absorption coefficient in the fundamental absorption region was determined from the transmission spectra as a function of frequency ν using the relation:

$$\alpha(h\nu) = \left(\frac{1}{t}\right)\ln\left(\frac{1}{T}\right) \qquad \text{Eq. [4.7]}$$

where t is the film thickness and T the transmittance of the film [54].

The absorption coefficient versus *hv* is given in Figure 4.33 and 4.34 for thin films which were annealed at 350 °C and 400 °C, respectively. The best linear graph were obtained for $n = 1/2$ as shown in Figure 4.35 and 4.36 for these examples. In the high energy region of absorption edge, α^2 vs *hv* plot was taken as the prime evidence for direct band gap. The intercept of the straight line on the *hv* axis gives the band gap. The energy band gaps for these thin films which are annealed at 350 °C and 400 °C were found as 2.63 and 2.64 eV, respectively.

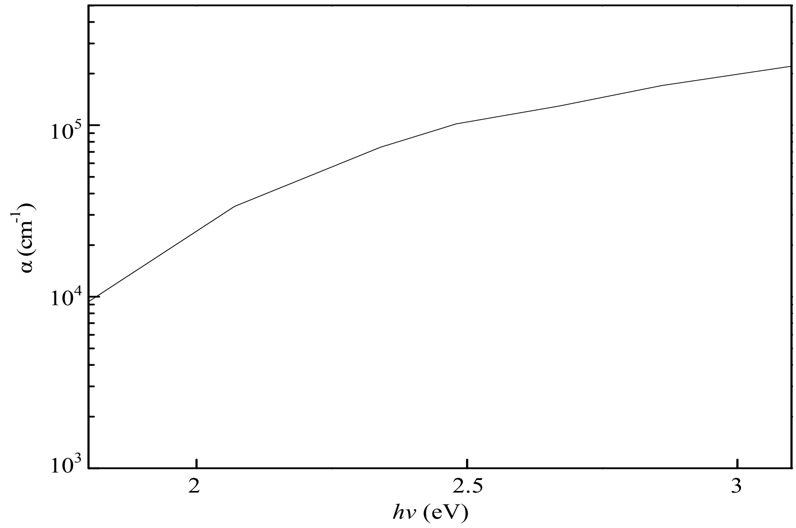

Figure 4.33. The change in absorption coefficient with changing *hv* of maghemite thin film annealed at 350 °C.

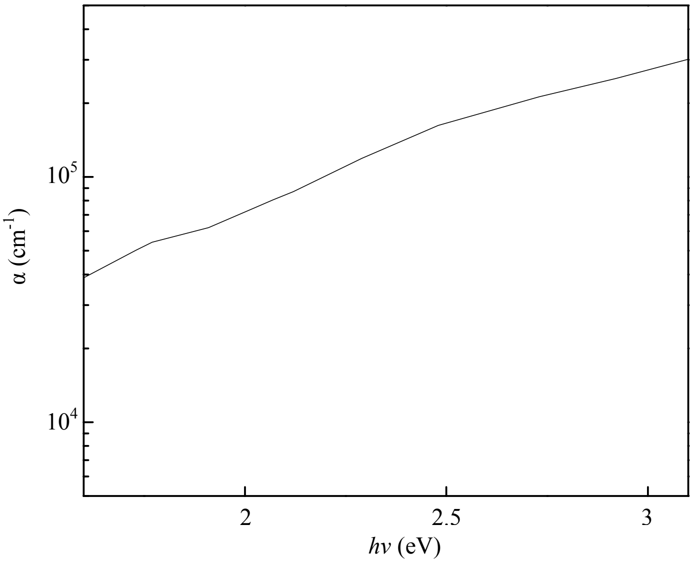

Figure 4.34. The change in absorption coefficient with changing *hν* of thin film annealed at 400 °C.

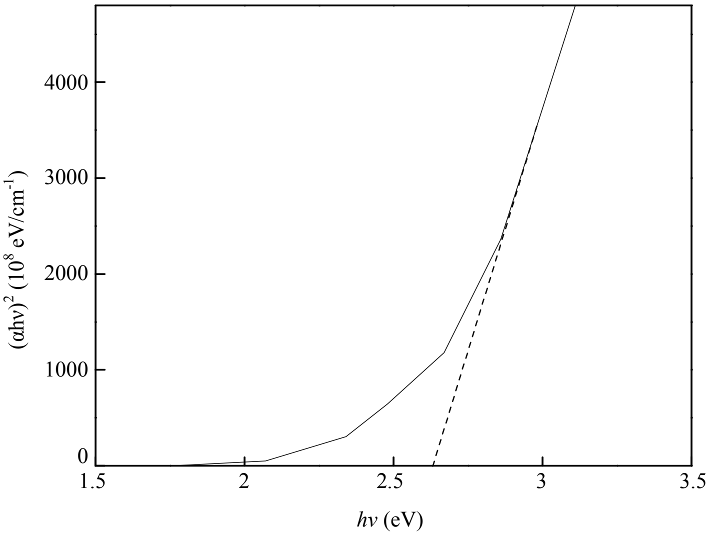

Figure 4.35. Plot of $(\alpha h\nu)^2$ versus photon energy of maghemite thin film annealed at 350 °C.

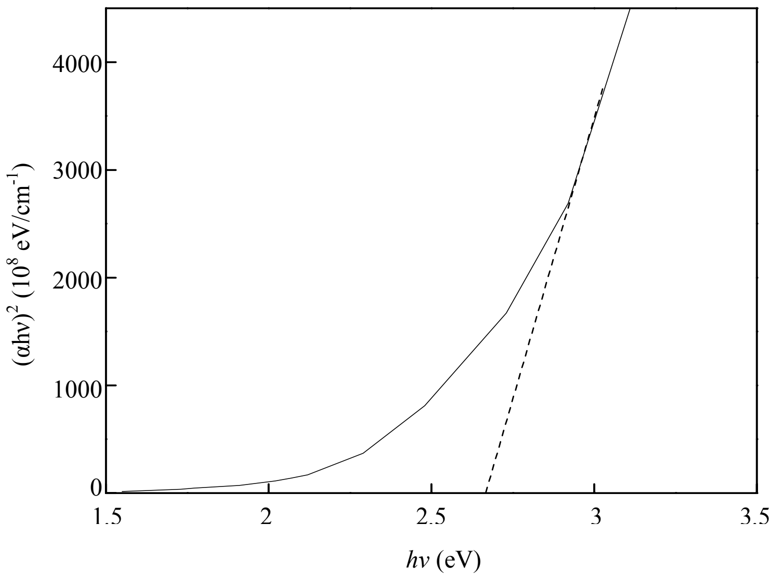

Figure 4.36. Plot of $(\alpha h\nu)^2$ versus photon energy of thin film annealed at 400 °C.

The E_g for hematite films is between 2.1-2.2 eV [38] whereas it is higher for maghemite thin films. Optical properties of maghemite thin films was not studied in detail in the literature but the expected value for optical band gap of maghemite phase is larger than 2.46 [61]. Some optical band gap values which were stated in the literature for different iron oxide thin films were given in Table 4.6. The calculated E_g values of the films which were annealed at 350 °C and 400 °C were close to optical band gap of the maghemite phase and they are also very close to each other. Thus, the film annealed at 400 °C is confirmed as a maghemite thin film like the film which was annealed at 350 °C for 1 hour.

Table 4.6. Literature survey for optical band gaps of different iron oxides

Iron oxide type	**Maghemite**	**Hematite**	**Magnetite**	**Amorphous Fe_2O_3**
E_g	2.46-3.00, (2.4) eV	2.1-2.2 eV	0.3 eV	1.91-1.93 eV
Reference no	61 , (62)	38	62	14

The extinction coefficients of the samples which were annealed at 350 °C and 400 °C were also calculated by simple relation between absorption coefficient and extinction coefficient which is given as [54]:

$$\alpha = 4\pi k / \lambda \qquad \text{Eq. [4.8]}$$

The extinction coefficient versus wavelength graphs of the samples annealed at 350 °C and 400 °C are given in Figures 4.37 and 4.38, respectively.

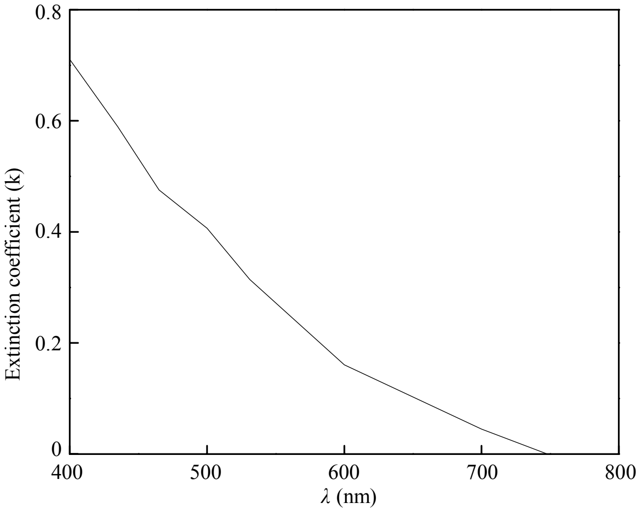

Figure 4.37. Extinction coefficient versus wavelength of maghemite thin film annealed at 350 °C.

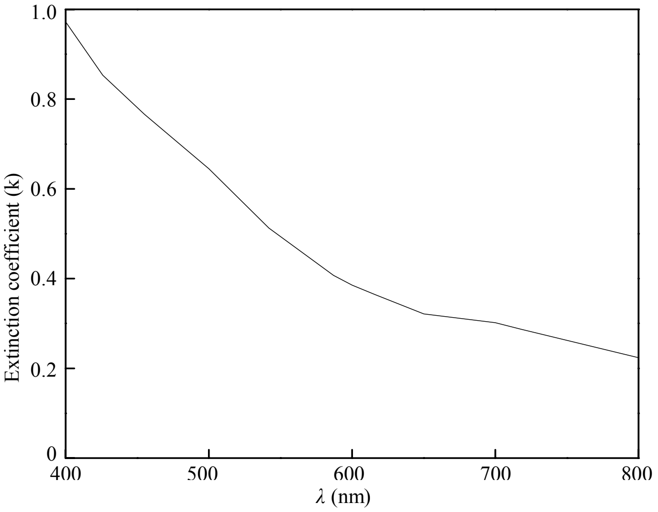

Figure 4.38. Extinction coefficient versus wavelength of maghemite thin film annealed at 400 °C.

To compare the optical band results of the maghemite thin film with thin film which was annealed at 500 °C, similar calculations were performed. However, the film annealed at 500 °C showed different behavior than other samples as it can be seen from the Figure 4.31. From the transmittance (%) – wavelength (λ) curve (Figure 4.39), optical parameters were also found such as the refractive index (n), absorption coefficient (α) and extinction coefficient (k) by modified envelope method. Moreover, reverse calculations were applied to found the thickness of the thin film.

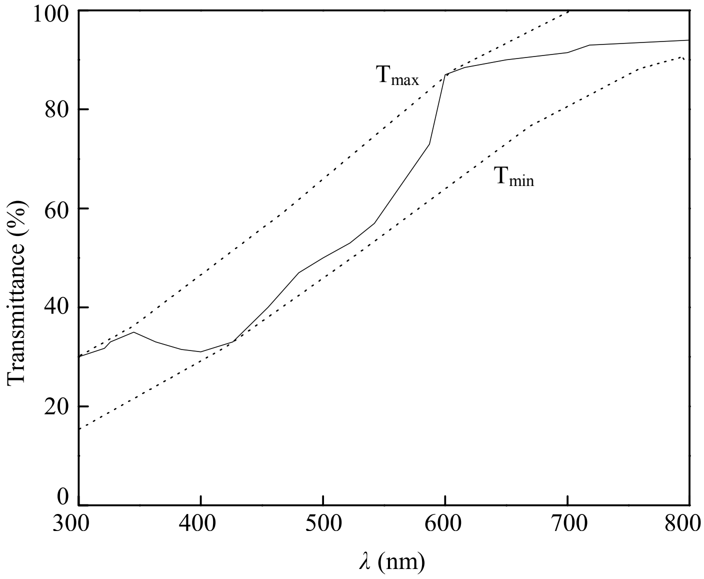

Figure 4.39. Optical transmission spectra of the thin film annealed at 500 °C, on glass substrate.

The refractive index of the film was calculated using equations [3.14] and [3.15]. From the optical parameters of $T_{\max}$, $T_{\min}$ and n_s which are known for the 630 nm wavelength (the wavelength of a He-Ne laser), the refractive index of the film was found as 2.92 which fits approximately to the refractive index value of the hematite which is ~3.0 in the literature [62] . The refractive index of glass substrate was taken as 1.52 [63].

From the equation [3.16], the thickness of the film annealed at 500 °C was calculated as 81 nm which was close to the thickness observed in SEM micrographs (80 nm) (Figure 4.12-4.13).

Absorption coefficient of the film annealed at 500 °C for 1 hour was calculated as 1.179×10^{-2} nm^{-1} by using equations [3.8] and [3.13] and the extinction coefficient of the same film was calculated as 0.59 by using equation [4.8] (Table 4.7).

Table 4.7. Optical properties of thin film annealed at 500 °C for 1 hour.

Thickness (nm)	**Refractive index (n)**	**Absorption coefficient (α) (nm^{-1})**	**Extinction coefficient (k)**
81	2.92	$1.179*10^{-2}$	0.59

4.6. Magnetic Properties of Maghemite Thin Films

Maghemite is a spinel type ferrimagnet with a Neel temperature well above 600 °C [64]. As the grain size becomes smaller, a critical size is reached at which magnetic characteristics of retentivity and coercivity vanish. Such magnetic property is called as superparamagnetic [65] which was explained in chapter 2. The magnetization curve of a three-layered maghemite thin film (~200 nm) which was annealed at 350 °C for 1 hour as a function of applied magnetic field is given in Figure 4.40. The graph shows no hysteresis that is both retentivity and coercivity are zero consistent with superparamagnetic behavior and nanostructured nature of the film. At 5 KOe the film had a magnetic saturation moment of $1.5.10^{-5}$ emu (8 emu/cm^3, 3 emu/g). The magnetization is also given per cm^3 and per grams in Figure 4.40 in order to compare the literature results. Some magnetization values of the maghemite thin films, which were indicated in the literature, are given in Table 4.8.

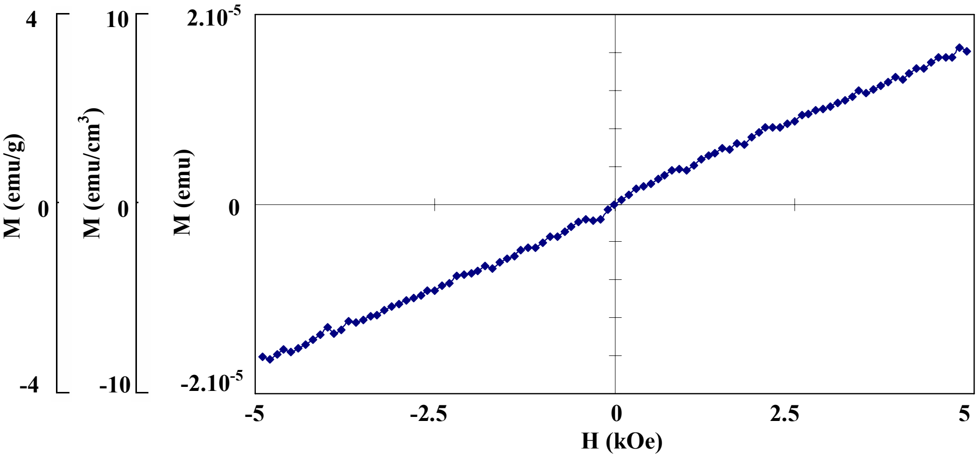

Figure 4.40. The M - H curve of maghemite thin film (~200 nm) annealed at 350 °C for 1 hour.

Table 4.8. Literature survey for saturation magnetization of maghemite thin films.

Saturation magnetization	52 emu/g	260 emu/cm^3	13.3 emu/g
Applied field	20 kOe	10 kOe	15 kOe
Ref no	31	7	66

In vibrating sample magnetometer (VSM) the signal magnitude is directly proportional to t, hence as the film thickness decreases it becomes more difficult to extract the signal of interest [67]. The magnetic disagreement between the resultant magnetic saturation value and the literature results may come from the limitation of the VSM equipment since the thicknesses of produced films were very thin.

The magnetic measurement of the thin film (~80 nm) which was annealed at 600 °C for 1 hour is given in Figure 4.41. From TEM and XRD, it is known that 600 °C is far above the maghemite - hematite transition temperature. As a result, the superparamagnetic behavior disappeared in the figure because of this transition. The weak magnetic behavior of the film is verified the presence of the hematite phase.

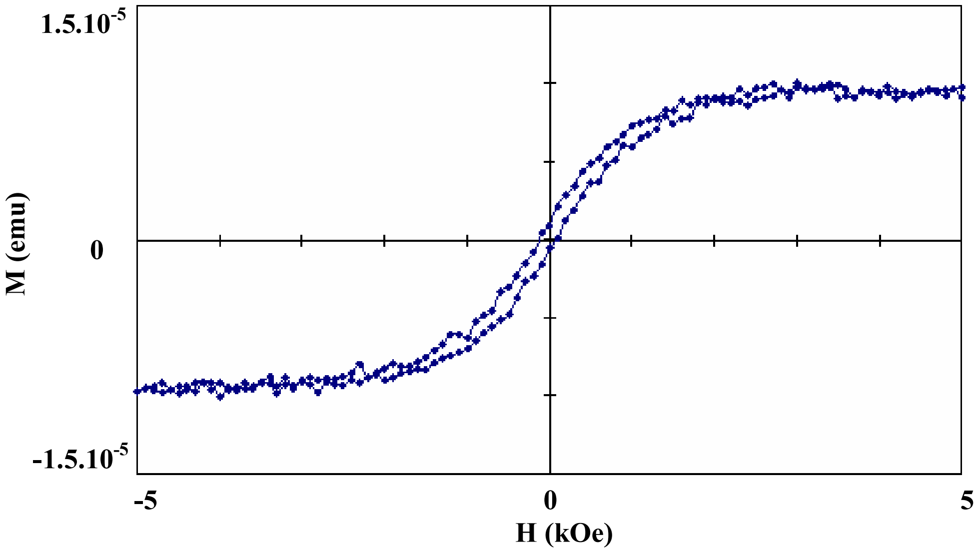

Figure 4.41. The M – H curve of single layered thin film (~80 nm) annealed at 600 °C for 1 hour.

CHAPTER 5

CONCLUSION AND FURTHER SUGGESTIONS

Some main results can be stated as follows;

The results showed that both solution properties and experimental parameters, which are annealing temperature, annealing time and film thickness, affect maghemite thin film formation.

Main solution, which behaves as Newtonian, assures the homogeneity of the film. Viscosity of the main solution found as 0.0035-0.0031 Pa.s which is lower than other viscosity results given in literature. The low viscosity yields low film thickness. As a result, thinner films were produced in this study than films produced in literature.

Maghemite can be easily transformed to hematite phase above 400 °C since maghemite phase is an unstable iron oxide phase. Maghemite thin film formation is achieved by producing single layer films (65 nm and 80 nm) for low annealing time (1 hour) at constant annealing temperature. With increasing annealing time and film thickness, maghemite transforms to hematite. The experiment evidence at 350 °C annealing temperature showed that at 1 hour annealing time, formation of maghemite thin film is observed at lower initial thickness; i.e. 80 nm for 1400 rpm spinning rate.

TEM results verified the presence of the maghemite phase by electron diffraction and selected area electron diffraction (SAED) methods, although maghemite phase was not detected by XRD because of very low thicknesses of the films. Lattice parameter of the maghemite thin film was found as 8.311 Å by using selected area electron diffraction method. This value is in the theoretical maghemite lattice parameter range, which is between 8.3-8.38 Å.

Optical band gap energies of the maghemite thin films annealed at 350 and 400 °C for 1 hour were found as approximately 2.64 eV. These values are close to maghemite optical band gap values observed in literature studies (2.46 - 3.00 eV).

The saturation magnetization (M_s) value of the superparamagnetic maghemite film was found as $1.5\text{x}10^{-5}$ emu (8 emu/cm^3, 3 emu/g) at 5 kOe. Although these results are lower than theoretical values, low thickness of the film affected the measurement and caused low saturation magnetization. It should be also noted that if the applied magnetic field in the measurements was higher than 5 kOe, than higher saturation magnetization values can be achieved because it is known that with increasing applied magnetic field, saturation magnetization increases in superparamagnetic materials.

Different characterization methods verified the maghemite thin film production and gave the structural, morphological, optical and magnetic properties of the maghemite thin films. For further investigations, other characterization techniques can be used to understand the stability of the maghemite thin films. Spectroscopic analyses are good candidates for characterizing maghemite thin films. X-ray Photoelectron Spectroscopy (XPS) and Raman Spectroscopic analyses can be used but they have some limitations. For instance Raman spectroscopy will not be good enough to examine the maghemite thin films because of the thickness restrictions. Rather than Raman spectroscopy, micro-Raman spectroscopy should be used for maghemite thin films to overcome this difficulty.

As a final suggestion, alkali modification can be done in order to increase the stability of the maghemite thin films. There exist studies in the literature related to this topic and some of them achieved better magnetic, optical and structural properties than unmodified maghemite thin films.

REFERENCES

1. A.K. Gupta, M. Gupta, *Biomaterials,* 26, 3995(2005)
2. J. Lai,K.V.P. Shafi, *Journal of the American Chemical Society*, 125, 11470 (2003)
3. B.Pal, M.Sharon, *Thin Solid Films*, 379, 83 (2000)
4. Li-S. Lim, G.E. Jang, *Sensors And Actuators*, *B* 77 215 (2001)
5. S. Dhara, A. C. Rastogi, B.K. Das. *Journal Of Applied Physics*, 74, 7019 (1993)
6. S. Dhara, A. C. Rastogi, B.K. Das. *Bulletin of Materials Science*, 18, 989 (1995)
7. J.K. Lin, J.M. Sivertsen *Journal Of Applied Physics*, 57, 4000 (1985)
8. G.S. Lim, T.C. Huang *Journal Of Applied Physics*, 59, 3543 (1986)
9. Q. Chen, X-G. Li, *Materials Letters*, 31, 247 (1997)
10. B. Pal, M. Sharon, *Thin Solid Films*, 379, 83 (2000)
11. Y. Gao, S. A. Chambers, *Journal Of Crystal Growth*, 174, 446 (1997)
12. M.A Aegerter, *Structure and Bonding*, 12, 149 (1996)
13. C.J. Brinker, G.W. Scherer, *Sol-Gel Science*, 23, 180 (1990)

14. N. Ozer, F. Tepehan, *Solar Energy Materials and Solar Cells*, 56, 141 (1999)

15. Lisa C. Klein, *Sol-gel processing of Advanced Materials,* American Ceramic Society, Ohio (1998)

16. Chuanbao Cao, Ming Luo, Hesun Zhu, *Journal of Non-Crystalline Solids*, 254, 146, (1999)

17. U. Schwertmann, R.M. Cornell, *Iron Oxides in the Laboratory : Preparation and Characterization*, VCH, New York (1991)

18. German Salazar-Alvarez, *Synthesis, Characterization and Applications of Iron Oxide Nanoparticles*, Ph.D. Thesis, Supervisor Prof. Dr. A. Zargorodni, University of KHT, Sweden , (2004)

19. T. Hashimoto, T. Yamata, *Journal of Applied Physics,* 80, 3184 (1996)

20. Magcraft Advanced Magnetic Materials, *http://www.rare-earth-magnets.com/magnet_university/magnetism.htm*, Magnetism, 03.10.2006

21. Electro-Patent-Invent, *http://www.patent-invent.com/electricity/inventions/paramagnetism.html*, Paramagnetism, 03.10.2006

22. K. J. Klabunde, *Nanoscale Materials in Chemistry*, Wiley-Interscience, New York (2001)

23. Nanotechnology for Engineers, *http://lmis1.epfl.ch/webdav/site/lmis1/shared/Files/Lectures/Nanotechnology%20for%20engineers/Archives/2004_05/Superparamagnetism.pdf*, Superparamagnetism, 03.10.2006

24. C. Cannas, G. Concas, D. Gatteschi, *Journal of Materials Chemistry*, 12, 3141, (2002)

25. Alain C. Pierre, *Introduction to Sol-Gel Processing*, Kluwer Academic Publishers, New York (2002)

26. Edward J.A. Pope, Sunnio Sakka, *Sol-Gel Science and Technology*, American Ceramic Society, Ohio (1994)

27. University of California, www-cms.llnl.gov, Chemistry and Material Science, 03.10.2006

28. J.D. Mackenzie, D.R. Ulrich, *In Ultrastructure Processing of Advanced Ceramics*, Wiley, New York (1988)

29. R.C. Mehrotra, *Journal of Non-Crystalline Solids*, 121, 1 (1990)

30. C. Jeffrey Brinker, *Sol-Gel Science*, Academic Press, Boston (1993)

31. John B. Wachtman, Richard A. Haber, *Sol-Gel Derived Ceramic Coatings*, Noyes Publications, NJ (1993)

32. Ege İzgi, *Characterization of Superconducting Bi-Sr-Ca-Cu-O System Prepared by Sol-Gel Processing*, M.S. Thesis, Supervisor Prof. Dr. Macit Özenbaş, Middle East Technical University, Turkey, (1996)

33. M. Sedlar, *Ceramics International*, 20, 73 (1994)

34. N. Takahashi, N. Kakuta, *Journal of Material Science*, 26, 497 (1991)

35. K. Yamaguchi, T. Fujii, S. Kuranoachi, *IEEE Transactions on Magnetics*, 25 3321 (1989)

36. T. Hashimoto, T. Yamata, *Journal of Applied Physics*, 80, 3184 (1996)

37. P. Lottici, C. Baratto *Optical Materials*, 9, 368 (1998)

38. P. Chauhan, S. Annapoorni, S. K. Trikha, *Bullettin of Material Science*, 21, 381 (1998)

39. A. Avila, G. Carbajal, A. Tiburcio, *Revista Mexicano de Fisica*, 49, 219 (2003)

40. N.J. Tang, *Journal of Magnetism And Magnetic Materials*, 282, 92 (2004)

41. H. S. W. Chang, Chuei-Chang Chiou, *Journal Of Solid State Chemistry*, 128, 87 (1997)

42. M. Sedlar, V. Matejec, *Journal of Sol-Gel Science and Technology*, 2, 587 (1994)

43. Burkan Kaplan, *Preparation of PLZT Thin Films By Chemical Solution Deposition and Their Characterization*, M.S. Thesis, Supervisor Prof. Dr. Macit Özenbaş, Middle East Technical University, Turkey, (2005)

44. D.E. Bornside, C.W. Macosco, L.E. Scriven, *Journal of Imaging Techology*, 13, 122 (1987)

45. Clarkson University, www.clarkson.edu/subramanian/ch301/notes/nonnewtonian.pdf, Non-Newtonian Fluids, 03.10.2006

46. M. J. Shah, E. E. Petersen, *Journal of Applied Physics,* 31, 963 (1960)

47. A. Jenekhe, S. B. Schuldt, *Industrial Engineering Chemical Fundamentals*, 23, 432 (1984)

48. Faruk Altan Yıldırım, *PZT Films on Stainless Steel by Chemical Solution Deposition*, M.S. Thesis, Supervisor Prof. Dr. Macit Özenbaş, Middle East Technical University, Turkey, (2002)

49. K. J. Gallagher, W. Feitknecht, U. Mannweiler, *Nature*, 217, 1118 (1968)

50. G. M. da Costa, E. De Grave, P. M. A. de Bakker, *Journal of Solid State Chemistry* ,113, 405 (1994)

51. Jerald A. Britten, Ian M. Thomas, *Journal of Applied Physics,* 71, 972 (1992)

52. University of Maryland, http://www.enma.umd.edu/LAMP/Sop/Piranha_SOP.htm, Laboratory for Advanced Material Processing, 03.10.2006

53. C.H. Hoa, Y.S. Huanga, P.C. Liaob, *Journal of Physics and Chemistry of Solids*, 60, 1797 (1999)

54. J C Manifacier, J Gasiot, J P Fillard, *Journal of Physics E,* 9, 1002 (1976)

55. P. Deb, A. Basumallick, *Materials and Manufacturing Processes*, 21, 658 (2006)

56. H. P. Klug and L. E. Alexander, *X-Ray Diffraction Procedures*, Wiley and Sons, New York (1974)

57. David B. Williams and C. Barry Carter, *Transmission Electron Microscopy : a Textbook for Materials Science*, Plenum Press, New York (1996)

58. A R Burkin, *Chemical Hydrometallurgy: Theory and Principles,* Imperial College, UK (2001)

59. D. Bersani, P. P. Lottici and A. Montenero, *Journal of Raman Spectroscopy*, 30, 355 (1999)

60. F. Bentivegna, M. Nyvlt, *Journal of Applied Physics*, 85, 2271 (1999)

61. S. Chakrabarti, D. Ganguli, *Physica E*, 24, 333 (2004)

62. I. Balberg, J. I. Pankove, *Physical Review Letters*, 27, 596 (1971)

63. L. A. Ageev, E. I. Plavskaya, V. K. Miloslavski, *Optics and Spectroscopy*, 88, 784 (2000)

64. A. H. Morrish, *In Crystals: Growth, Properties, and Application*, Springer-Verlag, New York (1980)

65. C. P. Bean and J. D. Livingston, *Journal of Applied Physics*, 30, 120 (1959)

66. K. Kojima, M. Miyazaki, *Journal of Sol-Gel Science and Technology*, 8, 77, (1997)

67. L. Jeffrey, D. Brad, *IEEE Transactions on Magnetics*, 40, 2191, (2004)